

THE SPLASH SURVEY: SPECTROSCOPY OF 15 M31 DWARF SPHEROIDAL SATELLITE GALAXIES*

ERIK J. TOLLERUD¹, RACHAEL L. BEATON^{2,10}, MARLA C. GEHA³, JAMES S. BULLOCK¹, PURAGRA GUHATHAKURTA⁴, JASON S. KALIRAI^{5,6}, STEVE R. MAJEWSKI^{2,10}, EVAN N. KIRBY^{7,11}, KAROLINE M. GILBERT^{8,11}, BASILIO YNIGUEZ¹, RICHARD J. PATTERSON^{2,10}, JAMES C. OSTHEIMER^{2,10}, ABRAR CHOUDHURY⁹

Draft version August 13, 2022

ABSTRACT

We present a resolved-star spectroscopic survey of 15 dwarf spheroidal (dSph) satellites of the Andromeda Galaxy (M31) as part of the Spectroscopic and Photometric Landscape of Andromeda’s Stellar Halo (SPLASH) project. We filter foreground contamination from Milky Way (MW) stars, noting that MW substructure is evident in this contaminant sample. We also filter M31 halo field giant stars, and identify the remainder as probable dSph members. We then use these members to determine the kinematical properties of the dSphs. For the first time, we confirm that And XVII, XXI, and XXII show kinematics consistent with bound, dark matter-dominated galaxies. From the velocity dispersions for the full sample of dSphs we determine masses, which we combine with the size and luminosity of the galaxies to produce mass-size-luminosity scaling relations. With these scalings we determine that the M31 dSphs are fully consistent with the MW dSphs, suggesting that the well-studied MW satellite population provides a fair sample for broader conclusions. We also estimate dark matter halo masses of the satellites, and find that there is no sign that the luminosity of these galaxies depends on their dark halo mass, a result consistent with what is seen for MW dwarfs. Two of the M31 dSphs (And XV, XVI) have estimated maximum circular velocities smaller than 12 km/s (to 1σ), which likely places them within the lowest mass dark matter halos known to host stars (along with Boötes I of the MW). Finally, we use the systemic velocities of the M31 satellites to estimate the total mass of the M31 halo: within 139 kpc, M31’s mass is $8.0^{+4.1}_{-3.7} \times 10^{11} M_{\odot}$ corresponding to a virial mass for M31’s dark matter halo of $1.2^{+0.9}_{-0.7} \times 10^{12} M_{\odot}$, consistent with previous results.

Subject headings: Galaxies: Local Group, Galaxies: dwarf, galaxies: kinematics and dynamics, galaxies: fundamental parameters, dark matter

1. INTRODUCTION

¹ Center for Cosmology, Department of Physics and Astronomy, The University of California at Irvine, Irvine, CA, 92697, USA; etolleru@uci.edu, bullock@uci.edu, byniguez@uci.edu

² Department of Astronomy, University of Virginia, P.O. Box 3818, Charlottesville, VA 22903, USA; rlb9n@virginia.edu, srm4n@mail.astro.virginia.edu, ricky@virginia.edu, james.ostheimer@gmail.com

³ Astronomy Department, Yale University, New Haven, CT 06510, USA; marla.geha@yale.edu

⁴ University of California Observatories/Lick Observatory, University of California at Santa Cruz, Santa Cruz, CA 95064, USA; raja@ucolick.org

⁵ Space Telescope Science Institute, 3700 San Martin Drive, Baltimore, MD 21218, USA; jkalirai@stsci.edu

⁶ Center for Astrophysical Sciences, Johns Hopkins University, Baltimore, MD, 21218

⁷ California Institute of Technology, 1200 East California Boulevard, MC 249-17, Pasadena, CA 91125, USA; enk@astro.caltech.edu

⁸ Department of Astronomy, University of Washington, Box 351580, Seattle, WA 98195, USA; kmgilber@u.washington.edu

⁹ Bellarmine College Preparatory, 960 West Hedding Street, San Jose, CA 95126, USA

¹⁰ Visiting Astronomer, Kitt Peak National Observatory, National Optical Astronomy Observatory, which is operated by the Association of Universities for Research in Astronomy (AURA) under cooperative agreement with the National Science Foundation.

¹¹ Hubble Fellow

* The data presented herein were obtained at the W.M. Keck Observatory, which is operated as a scientific partnership among the California Institute of Technology, the University of California and the National Aeronautics and Space Administration. The Observatory was made possible by the generous financial support of the W.M. Keck Foundation

Dwarf Spheroidal (dSph) galaxies are among the most extreme objects in the pantheon of galaxies. Their low luminosities ($10^3 < L/L_{\odot} < 10^8$), lack of significant gas (Greivich & Putman 2009), and low numbers compared to Λ CDM expectations (Klypin et al. 1999; Moore et al. 1999) are all puzzles that remain to be solved. The difficulty in understanding the count of dSph galaxies around the Milky Way and M31 is known as the Missing Satellites Problem, an issue that has prompted a flurry of activity modeling these galaxies (recently, Kravtsov 2010; Bullock 2010; Kazantzidis et al. 2011a; Font et al. 2011, and references therein). Most models rely heavily on feedback scenarios that are tied directly to the masses of the dark matter halos that presumably host dSph galaxies. In this sense, mass determinations for dwarfs are among the most important diagnostic measurements for testing theoretical predictions at the frontier of galaxy formation.

While the brightest dSphs can be detected at the distance of nearby clusters (e.g., Hilker et al. 2003; Durrell et al. 2007), faint, diffuse dSphs can only be detected via resolved star counts, which limits detection to the Local Group (LG). Kinematics of these galaxies thus requires resolved star spectroscopy at extragalactic distances. Thus, despite the motivations outlined above, detailed study of a large population of dSphs has been limited to the MW satellites (e.g., Mateo 1998; Simon & Geha 2007; Walker et al. 2009; Simon et al. 2011).

Studies of the MW dSph population have resulted in puzzles that have provided interesting challenges to

Λ CDM and galaxy formation models. The missing satellite problem noted above is the classic example, for which a variety of solutions have surfaced (e.g., Bullock et al. 2000; Strigari et al. 2007; Tollerud et al. 2008; Bovill & Ricotti 2009; Koposov et al. 2009; Kravtsov 2010). However, there remain other questions such as the cause of their low gas fractions (Grcevich & Putman 2009; Nichols & Bland-Hawthorn 2011), their morphologies (Kazantzidis et al. 2011b), or the curiously small number with high densities expected by Λ CDM (Boylan-Kolchin et al. 2011). These studies are based entirely on the MW dSph population, as this has been the only available dataset. Yet there is evidence that the MW has had an unusual merger history relative to similarly bright galaxies such as M31 (Guhathakurta et al. 2006; Hammer et al. 2007). Furthermore, there are hints that the dSph populations of M31 and the MW exhibit different scaling relations (McConnachie et al. 2005a; Kalirai et al. 2010). Hence, expanding the sample of systems is crucial to generalizing the information dSphs provide about galaxy formation.

Fortunately, the past few years have seen much growth in the known satellite population of M31. This is primarily due to the advent of deep surveys of the region surrounding M31 specifically designed to search for substructure like dSphs or their remnants (e.g., Ibata et al. 2007; McConnachie et al. 2009). While the distance to M31 means that detection limits do not reach those of the MW’s ultra-faint dSph system, smaller angular coverage is needed to survey M31’s environs. Thus, the full population of known M31 satellites (shown in Figure 1) now includes 27 dSphs (Zucker et al. 2004; Martin et al. 2006; Zucker et al. 2007; Majewski et al. 2007; Irwin et al. 2008; McConnachie et al. 2008; Martin et al. 2009; Richardson et al. 2011; Slater et al. 2011; Bell et al. 2011). These are further supplemented by 4 dwarf Elliptical (dE) satellites, which are similar in morphology to the dSph, but have somewhat higher luminosities.

The imaging surveys that detected these dSphs provide datasets that allow characterization of the photometric properties of M31 satellites, but do not provide the kinematics of these dSphs necessary for characterizing their masses and dark matter content. These kinematical datasets are also crucial for confirming the candidates’ status as self-bound galaxies. This is illustrated by two M31 dSphs (And IV and VIII) that were originally identified as dSph satellites, but were later shown by spectroscopic follow-up to be non-satellites (Ferguson et al. 2000; Ibata et al. 2004; Merrett et al. 2006). Beyond this, understanding the kinematics of M31 satellite system as a whole also provides insight into M31, its dark matter halo, and its accretion history (e.g., Evans et al. 2000; van der Marel & Guhathakurta 2008). While kinematics exist for some of the M31 dSphs (Côté et al. 1999; Guhathakurta et al. 2000; Chapman et al. 2005, 2007, 2008; Letarte et al. 2009; Collins et al. 2010; Kalirai et al. 2010), the large number of recent discoveries leave many yet to be spectroscopically confirmed, and a homogeneously observed and reduced sample of a significant fraction of these satellites is necessary to properly determine characteristics of the satellites system *as a whole*.

With these ends in mind, we report here on kinematics of 15 dSphs from the Spectroscopic and Photometric

Landscape of Andromeda’s Stellar Halo (SPLASH) Survey. This ongoing survey of the environs of M31 aims to characterize the stellar halo of M31 and its satellite population via resolved star spectroscopy. A companion paper on structural parameters and photometric properties is forthcoming (Beaton et al., in prep.).

This paper is organized as follows. In §2, we describe the observations performed for this data set. In §3, we describe the reduction and membership performed homogeneously across the spectroscopic data set, as well as our method for estimating total velocity dispersions for each satellite in the sample. In §4, we present the results of our full spectroscopic sample, and consider each satellite in turn, describing the results of our analysis and unique aspects of each galaxy. In §5, we consider the scaling relations of M31 dSphs and compare them to the MW. In §6, we use the galaxies’ v_{sys} to estimate the mass of M31. Finally, we present our conclusions in §7.

2. OBSERVATIONS

We provide an overview of the M31 satellite system in Figure 1. M31 is represented as the (orange) ellipse near the center, while the other symbols are likely M31 satellites. The 15 satellites presented here with Keck/DEIMOS spectroscopy of resolved stars are shown as filled (blue) triangles, while the remainder of the dSphs are shown as outlined (red) triangles (excepting the newly-discovered And XXVIII, which is much further out than the other dSphs). Also shown are M33 (cyan ellipse at lower left), and the dE satellites (black squares). From this census it is apparent that our sample includes over half of the dSphs in the M31 system, with the spatial unevenness only due to the very recent discovery of some of the dSphs. Also shown are lines of Galactic latitude, indicating significant variation in the MW foreground across M31’s environs.

We present 33 DEIMOS slitmasks covering 15 dSphs in M31, with mask details provided in Table 1. Eight of these masks have been presented elsewhere: the And I and III masks were previously presented in Kalirai et al. (2010), the And X data set was originally published by Kalirai et al. (2009), and 2 masks of And XIV were described by Majewski et al. (2007). There is an additional series of SPLASH slitmasks for And II that will be described in a forthcoming paper (Ho et al., in prep.). All masks were reduced and analyzed homogeneously using the procedure describe in the following sections, including those noted above that have been previously published.

The details of the imaging used for target selection will be described in detail in the companion paper (Beaton et al., in prep.). Here we summarize the particulars relevant for spectroscopic target selection. Our imaging is primarily in the Washington system (specifically, the M and T_2 filters), which we convert for some target selection purposes to Johnson-Cousins V,I using the relations of Majewski et al. (2000). We obtained additional imaging of the same fields with the DDO51 intermediate-band filter Majewski et al. (2000). This filter is centered near the surface-gravity dependent Mgb and MgH stellar absorption features, allowing it to discriminate between M31 giant stars and MW foreground dwarf stars. Thus, selecting targets in e.g., the $M - DDO51$ vs. $M - T_2$ color-color diagram allows for far more efficient selection

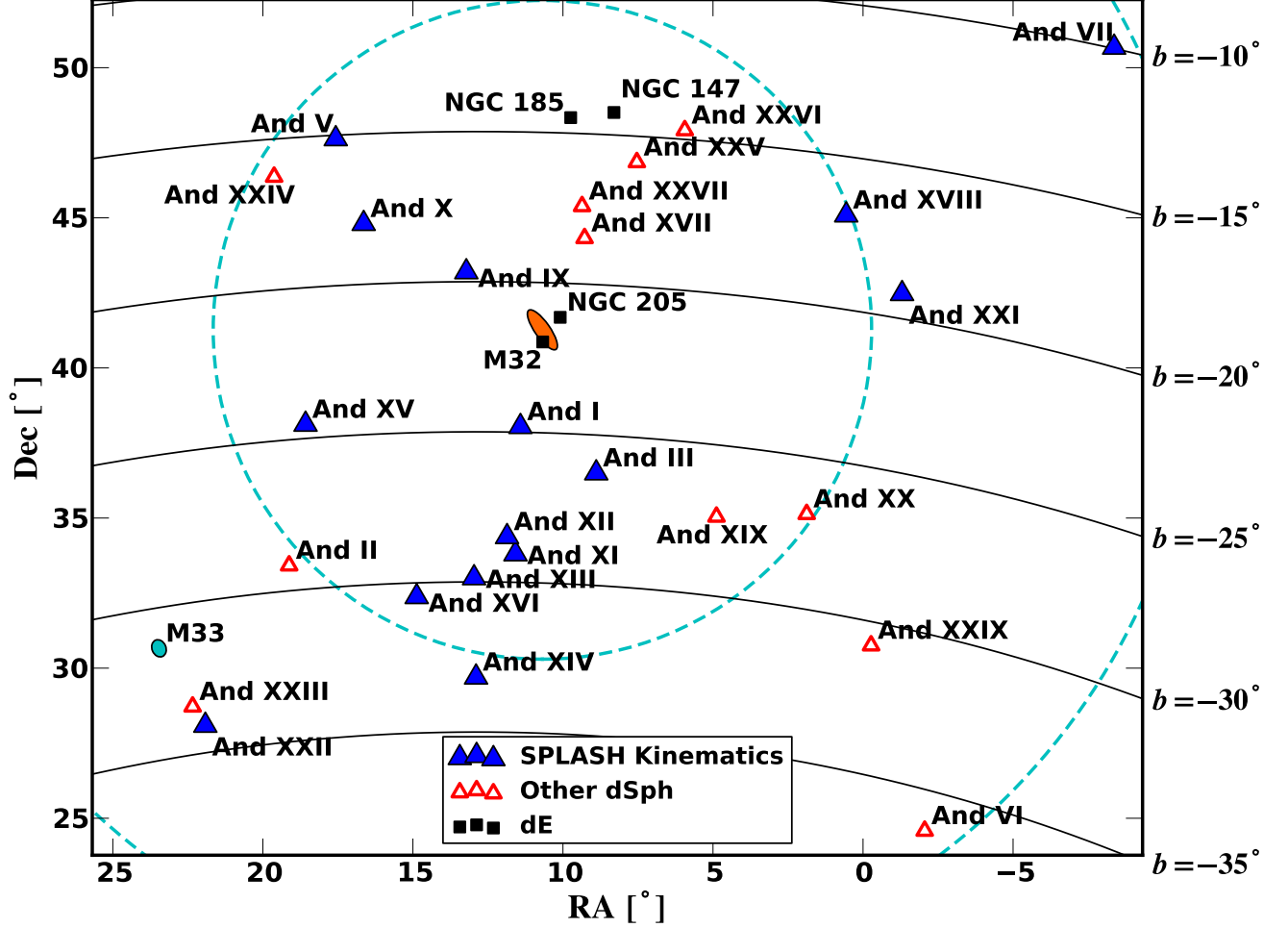


FIG. 1.— M31 and its satellites. M31’s disk is indicated by the (orange) ellipse in the center, and M33’s disk is the (cyan) ellipse at the lower-left. The dSph sample presented here are filled (blue) triangles, and the outlined (red) triangles are the other dSphs. Squares (black) are M31’s dE population. The two (cyan) dashed circles centered on M31, at projected radii of 150 and 300 kpc, represent the approximate extent of the PAndAS survey (McConnachie et al. 2009) and the virial radius of M31’s expected dark matter halo (Klypin et al. 2002), respectively. The (black) solid lines are lines of constant Galactic latitude.

of spectroscopic targets that have high probabilities of being giants (Kalirai et al. 2006; Guhathakurta et al. 2006; Gilbert et al. 2006).

We selected stars for spectroscopic follow-up from catalogs generated from this imaging. Our candidates for each mask were selected by assigning priorities based on how far a given star was from a fiducial isochrone on the $M - T_2, T_2$ color-magnitude diagram (CMD). This is similar to the membership selection described in §3.2 and illustrated in the plots of §4, but with looser restrictions. We also assigned priorities based on how close a star was to the giant star locus in the $M - DDO51$ vs. $M - T_2$ color-color diagram (Ostheimer 2003). We demonstrate this part of the selection in Figure 2, showing stars for a representative field and indicating the loci of red giant stars (the targets) and main sequence stars (the contaminants), with points colored according to an estimate of the probability of the star being a giant. Because most M31 dSphs are smaller than the footprint of a DEIMOS slitmask ($\approx 16' \times 5'$), in most cases we aligned the mask such that the dSph was centered to one side of the slitmask. This allows for measurement at larger radii of M31

halo structure within which a satellite might be embedded (e.g., And I as described by Kalirai et al. 2010).

Note that the above description is valid for all masks except those targeted at And X, And XV, And XVI, And XVIII, and And XXII. For And X, Sloan Digital Sky Survey (SDSS) imaging was used for target selection (Adelman-McCarthy et al. 2006), for And XV and XVI selection was made using Canada France Hawaii Telescope (CFHT) archival imaging, while for the last two dSph we made use of B and V band imaging from the Large Binocular Telescope (Beaton et al., in prep.). For these, distance from a fiducial isochrone in a CMD was used without DDO51 pre-selection.

The spectroscopic setup for the DEIMOS observations used the 1200 lines mm^{-1} grating with a central wavelength of 7800 Å. This provides a spectral coverage over a range of 6400 - 9100 Å (for objects centered in the mask along the dispersion direction), with a FWHM resolution of ≈ 1.3 Å. This provides coverage of the Calcium triplet (CaT) stellar absorption feature near 8500 Å and (depending on the slit location) $H\alpha$ to facilitate identification and accurate radial velocity measurements. A

TABLE 1
OBSERVED DEIMOS SLITMASKS.

Target	Mask Name	MJD	UTC Date	Total Exposure Time (s)	No. of Slits	No. of Successful Velocities ^a
And I	d1.1	53679.31	11/5/2005	4055	150	71
And I	d1.2	53994.62	9/16/2006	3600	145	88
And III	d3.1	53621.34	9/8/2005	3600	119	88
And III	d3.2	53621.39	9/8/2005	3600	117	83
And III	d3.3	55066.56	8/23/2009	3600	123	30
And V	d5.1	54739.45	9/30/2008	3000	101	52
And V	d5.2	54739.55	9/30/2008	2250	105	64
And V	d5.3	54740.54	10/1/2008	2250	75	37
And VII	d7.1	54682.43	8/4/2008	3000	152	110
And VII	d7.2	54682.46	8/4/2008	1800	147	74
And IX	d9.1	55069.56	8/26/2009	2700	115	74
And IX	d9.2	55069.60	8/26/2009	2400	101	58
And X	d10.1	53618.39	9/5/2005	3600	82	51
And X	d10.2	53618.44	9/5/2005	3600	93	54
And XI	d11	55450.60	9/11/2010	3600	71	22
And XII	d12	55451.00	9/12/2010	3600	62	22
And XIII	d13.1	54739.37	9/30/2008	6000	66	18
And XIII	d13.2	54740.48	10/1/2008	4800	65	15
And XIII	d13.3	55450.31	9/11/2010	3600	107	18
And XIII	d13.4	55450.36	9/11/2010	5400	114	12
And XIII	d13.5	55450.44	9/11/2010	5400	115	11
And XIV	A170.1	54059.20	11/20/2006	3600	93	39
And XIV	A170.2	54060.20	11/21/2006	3600	88	36
And XIV	d14.3	55065.55	8/22/2009	3600	99	33
And XV	d15.1	55068.36	8/25/2009	3600	105	82
And XV	d15.2	55068.43	8/25/2009	4800	120	60
And XVI	d16.1	55068.50	8/25/2009	4800	92	29
And XVI	d16.2	55068.56	8/25/2009	3600	77	16
And XVIII	d18.1	55069.40	8/26/2009	10800	76	49
And XXI	d21.1	55710.56	5/29/2011	6905	96	12
And XXII	d22.1	55450.55	9/11/2010	3600	140	10
And XXII	d22.2	55451.56	9/12/2010	4800	76	7
And XXII	d22.3	55476.59	10/7/2010	3955	125	6

^a While for some masks there is an apparently low percentage of successful velocities, this is due to higher fractions of filler targets in the sparser fields that tend to have lower odds of being RGB stars. This is discussed in detail §3.1.

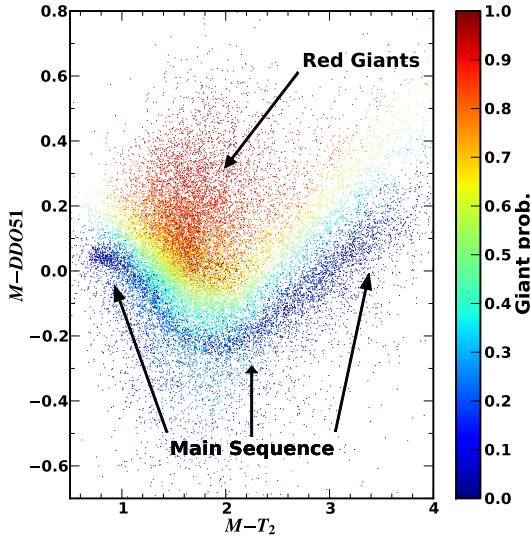


FIG. 2.— $M - T_2$, $M - DD051$ color-color diagram used for pre-selection of likely giant stars, for a representative field near And I. Points are colored by red giant probability determined by the method of Ostheimer (2003), which assigns high probabilities to stars near the indicated locus for stars with low surface gravity, while avoiding probable dwarf stars in the “swoosh” feature. Stars with high probability are selected for spectroscopic follow-up.

typical total integration time of 3600 s per mask provides a mean signal-to-noise ratio per pixel of ~ 7 for our entire sample. Signal-to-noise depends strongly on the target

star’s magnitude, so we plot in Figure 3 the variation of signal-to-noise varies with magnitude.

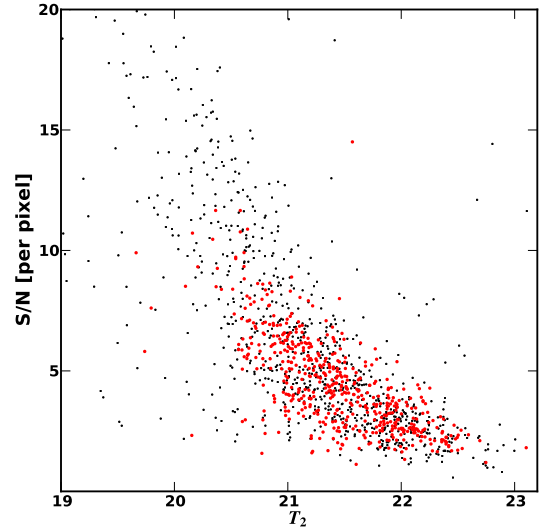


FIG. 3.— Per pixel signal-to-noise vs. T_2 -band magnitude for stars in this survey with successful spectra. Larger (red) circles are stars identified as likely dSph members following the prescription described in §3.2, while smaller (black) points are non-member stars.

3. SPECTROSCOPIC DATA ANALYSIS

Here we describe the procedure applied homogeneously to each slitmask (Table 1) to extract radial velocities from the spectroscopic data, and to determine each satellite’s kinematics.

3.1. *Keck/DEIMOS Data Reductions*

We make use of the spec2d DEIMOS reduction pipeline¹³ and modified versions of the spec1d and zspec analysis codes developed for the DEEP2 survey. To summarize, the pipeline first rectifies each slit spectrum along the spatial direction and corrects for the slit function and fringing using quartz lamp flats. It then determines a 2d wavelength solution from NeArKrXe arc lamp exposures taken for each mask. Science exposures are then combined with inverse variance weighting including cosmic ray rejection. Finally, 1d spectra are extracted using Horne (1986) optimal extraction.

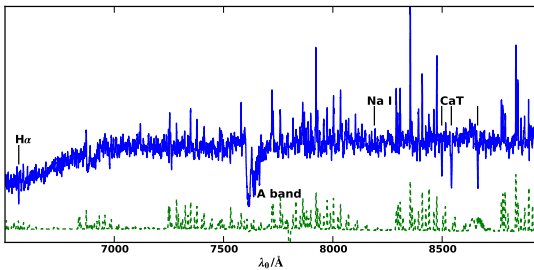


FIG. 4.— Example spectrum of a star with a high probability of dSph membership. Solid (blue) line is the spectrum (smoothed with a 4 pixel boxcar filter), while dashed (green) shows the error spectrum, peaking at strong sky emission lines. For this star, $I = 20.7$, and un-smoothed $S/N = 6$ per pixel.

The above procedure thus yields 1d spectra for each slit, an example of which is given in Figure 4. These spectra are then further analyzed to determine heliocentric radial velocities, following the same general procedure described by Simon & Geha (2007) (See also Guhathakurta et al. 2006 and Kalirai et al. 2010). The spectra are first re-binned into equally-spaced logarithmic bins of 15 km s^{-1} . These spectra are then cross-correlated with high signal-to-noise templates taken with DEIMOS using an identical setup as that described above. These templates include dwarf, subgiant, giant, and AGB stars. The largest subset are the giant templates, which range from spectral type F8 to M8, although most of our likely members best match early-K and late-G templates.

We then manually examine each spectrum and remove contaminant spectra that are clearly galaxies, as well as those for which no absorption features are visible, i.e., low signal-to-noise spectra. This process results in very different success rates from mask to mask, because masks with a low density of good M31 RGB candidates will include a large number of “filler” targets. These targets tend to be fainter by necessity, meaning the photometric errors are larger, and the fraction of background galaxies that overlap with the M31 RGB is much higher, increasing the contamination rate. Furthermore, even true RGB targets are fainter, and thus identification of absorption lines becomes more difficult, further lowering the success

rate. Together, these effects are the main reasons for the high variability in mask-to-mask success rates (i.e. the ratio of the last two columns in Table 1).

We also correct for mis-centering of stars in slits by matching to the A-band telluric feature as described by Simon & Geha (2007) and Sohn et al. (2007). This correction is crucial, as mis-centered stars for typical astrometric errors result in errors comparable to that of the internal velocity dispersion of the dSphs (see the discussion of Kalirai et al. 2010, Section 2.3). Finally, we correct the observed radial velocities to the heliocentric frame.

Understanding the errors on the radial velocity computed above is crucial to determining the internal velocity dispersion of the dSphs, and hence we determine the errors on each star by Monte Carlo simulation. For each spectrum that passes the inspection procedure described above, we generate 1000 realizations of the 1d spectrum, assuming independent, Poisson errors on each pixel based on the observed variance. For each of these realizations we compute the telluric correction and the cross-correlation radial velocity, and visually examine the histogram of radial velocities for these simulations. We reject any spectra that show multi-modal character in radial velocity (e.g., a secondary cross-correlation peak that is of comparable magnitude to the primary peak). We then fit a Gaussian to the primary peak and use the best-fit parameters as the radial velocity v_i and random error σ_r for each spectrum. Repeat measurements of stars for this spectroscopic setup are described in detail by Simon & Geha (2007) and Kalirai et al. (2010) Section 2.4, and our sample includes the same repeat measurements as the latter. Both sets of repeat measurements showed an additional systematic error component of 2.2 km s^{-1} . Thus, we adopt $\sigma_t \equiv \sqrt{\sigma_r^2 + (2.2 \text{ km s}^{-1})^2}$ as our final radial velocity error estimate for each spectrum.

We also measure equivalent widths (EW) for the Na I $\lambda 8190$ doublet ($\lambda 8183, 8195$), a surface-gravity dependent feature useful for dwarf/giant discrimination. We adopt a blue pseudo-continuum from $8155 - 8175 \text{ \AA}$, red $8203 - 8230 \text{ \AA}$, and a line bandpass of $8178 - 8200.5 \text{ \AA}$ (Schiavon et al. 1997). For these measurements, we determine errors using the same Monte Carlo realizations and Gaussian fitting procedure described above for radial velocities.

This procedure thus provides a sample of stellar spectra with heliocentric radial velocities (and corresponding errors estimates), as well as indices for spectral features that are typically detectable for red giants at the distance of M31. We match these spectra to the corresponding photometric measurements to create a catalog of candidate M31 dSph stars. This provides the input to our membership selection scheme, described below.

3.2. *Membership*

After determining the radial velocity for each star in our sample, we next determine whether it is a member of a dSph galaxy or a contaminant. There are two distinct populations of stellar contaminants: MW red dwarf stars (foreground), and M31 red giants (halo field stars). We consider each of these in turn and then describe our method for assigning membership probabilities to individual stars.

¹³ <http://deep.berkeley.edu/spec2d/>

Foreground contamination from MW stars is typically worse than the M31 component, particularly for dwarfs that lie at lower absolute Galactic latitudes than M31. Gilbert et al. (2006) describes a step-by-step approach for empirically determining the probability that a star is a MW contaminant or an M31 RGB star. While such an approach is valuable for searching for low density M31 halo field stars, the dSphs we consider here have much higher surface densities in their centers, and thus these diagnostics are less crucial near the centers of the satellite. Furthermore, given that the dSphs studied here exhibit low-dispersion kinematical “cold spikes” at velocities closer to M31’s system velocity than that of the MW, even a wide velocity window that extends into the tails of the satellite velocity distribution will overlap negligibly with the MW stars. This is borne out in the velocity histograms shown in §4, as the distributions from the Robin et al. (2003) model of the MW do not overlap with the velocity windows we adopt.

Halo field and spheroid stars from M31 also provide a significant source of contamination. While these are generally lower surface density than MW foreground, M31 contamination is more problematic for selecting dSphs due to two effects. First, the DDO51 pre-selection technique described above is only effective at eliminating foreground dwarf stars — M31 halo field red giants cannot be distinguished from M31 dSph red giants with DDO51. Second, while the velocity distribution of the M31 halo is much broader than that of the dSphs, it overlaps with the dSph distributions for many of the satellites. Hence, there is no definitive way to exclude M31 halo field stars from the dSphs with radial velocity measurements. Indeed, given the hypothesis that the outer reaches of galactic halos or spheroids are formed from dissolved satellites (e.g., Bullock & Johnston 2005; Guhathakurta et al. 2006), it is unsurprising that the halo’s stellar properties overlap with those of the satellites.

Fortunately, the surface densities of M31 halo field stars in the environs of these satellites are quite low relative to the dSphs. M31’s spheroid (non-disk) component can be decomposed into two sub-components: an “inner spheroid” that extends to ~ 30 kpc and features a de Vaucouleurs profile, and a power-law “halo” component with a slope of ~ -2.3 out to at least 160 kpc (Guhathakurta et al. 2005). All of our dSph fields, aside from And I and IX (see §4.1 and 4.5), lie firmly in the halo regime, and the distances imply at most a few halo field stars per DEIMOS slitmask (Guhathakurta et al. 2005, 2006; Gilbert et al. 2007). Hence, the probability of finding such a star near the center of a dSph with a similar velocity to that of the member stars is low. Additionally, some of the dSphs have systemic velocities well separated from the M31 spheroid — the M31 halo distribution is centered at ~ -300 km s $^{-1}$ with a dispersion of ~ 100 km s $^{-1}$ (Guhathakurta et al. 2005, 2006; Chapman et al. 2006; Gilbert et al. 2007). Furthermore, the metallicity distribution functions of the M31 halo and the dSphs are partially disjoint. M31 dSphs examined here tend to have metallicities in the range $[\text{Fe}/\text{H}] \sim -1.4$ to -2.0 (Martin et al. 2006; McConnachie et al. 2008; Martin et al. 2009; Kalirai et al. 2010), while the M31 spheroid is more concentrated in the range $[\text{Fe}/\text{H}] \sim -1.5$ to -0.1 (Guhathakurta et al.

2005, 2006; Chapman et al. 2006). While there is overlap, particularly in the outer halo where M31 metallicities are lower, the distributions are reasonably separated in the mean. Thus, metallicity-based criteria have hope of approximately separating M31 halo structure from dSph stars in the outskirts of the satellites. While we do not make use of spectroscopic metallicities due to the lower signal-to-noise for some of our spectra, our selection depends on this metallicity distinction implicitly through color-magnitude diagram selection.

With these two sources of contamination in mind, we adopt a method for determining membership probabilities that depends only on distance from the center of the target satellite and location in the $(T_2, M - T_2)$ color-magnitude diagram (CMD). Explicitly, the membership probability for each star in the survey is calculated as

$$P_{\text{memb}} = \exp \left(-\frac{\Delta\alpha^2 + \Delta\delta^2}{2\eta R_{\text{eff}}^2} - \frac{\Delta(M - T_2)^2}{2\sigma_c} - \frac{\Delta T^2}{2\sigma_m} \right) \times \left(\frac{\arctan[-10(\Sigma_{\text{Na}} - 2)]}{\pi} + \frac{1}{2} \right), \quad (1)$$

where $\Delta\alpha$ and $\Delta\delta$ are the circular distance from the star to the center of the dSph (in RA and Dec, respectively), $\Delta(M - T_2)$ and ΔT are distances from fiducial isochrones in the $(T_2, M - T_2)$ CMD, R_{eff} is the dSph’s half-light radius, Σ_{Na} is the Na I equivalent width, and η , σ_c , and σ_m are free parameters.

The first term of this expression simply assigns a circular Gaussian spatial distribution of probabilities, weighting the region inside the half-light radius. While some of the dSphs have elliptical light distributions, here we use a circular distribution to avoid introducing biases for the cases where the ellipticity is not well measured. In most cases, we adopt $\eta = 1.5$, except in cases where halo contamination is much different from typical as indicated by the velocity distribution at large distances from the satellite. In these cases we sometimes use a slightly different η value to down- or up-weight the membership probability for stars beyond R_{eff} . The satellites for which this is done are explicitly mentioned in §4.

The latter two terms inside the exponential define Gaussian acceptance regions around the fiducial isochrone. We make use of Girardi et al. (2002) isochrones for the Washington photometric system¹⁴ for a range of metallicities from $[\text{Fe}/\text{H}] = -2.2$ to -1.0 with 12 Gyr ages, offset by the distance modulus of the satellite. We then correct the M and T_2 photometry for Galactic extinction/reddening using the Schlegel et al. (1998) dust maps, and use photometry of the DDO51-selected stars within each dwarf’s half light radius to empirically choose the best-fitting isochrone. With these likely members as a guide, we adopt fiducial values of $\sigma_c = 0.1$ and $\sigma_m = 0.5$, although these parameters are adjusted for some dwarfs, as described in §4.

Given that the only stars we can reach spectroscopically at the distance of M31 are red giant stars, which form a nearly vertical sequence in the CMD, the range of accepted colors, encoded in σ_c , contains contributions from both intrinsic metallicity scatter and photometric

¹⁴ <http://stev.oapd.inaf.it/cgi-bin/cmd>

errors. Meanwhile, σ_m contains both distance and photometric uncertainties. Uncertainty in the age of the stellar population induce further degeneracy in metallicity and distance. This motivates the choice of fitting isochrones empirically rather than performing a detailed analysis of the isochrone-inferred metallicities, leaving such discussion to the companion paper (Beaton et al., in prep.). We instead use the isochrones primarily to reject M31 halo field stars (which have a disjoint metallicity distribution, as described above). This membership approach is thus not sensitive to specific assumptions regarding metallicity or age of the stellar populations, and has been found to be successful for both M31 dSphs (Kalirai et al. 2010; Collins et al. 2010) and MW dSphs (Simon & Geha 2007; Simon et al. 2011). As the plots in §4 show, these isochrones closely follow the spectroscopically apparent cold velocity spikes present for most of the satellite fields, validating the approach.

The arctan term serves to favor stars that have Na I $\lambda 8190$ values more consistent with RGB stars than those on the main sequence. This feature is surface gravity sensitive and hence is usually very weak or undetectable in M31 RGB stars, while clearly apparent even on visual inspection of a spectrum of a cool (foreground) dwarf star. This feature becomes weaker for hotter stars, however, and hence only rejects the cooler MW dwarf stars. The particular functional form is chosen to smoothly transition from 0 to 1 with an adjustable center and sharpness of transition. While the center (here chosen as 2) and sharpness (10) are nominally free parameters, they should not depend on the particulars of any dSph, but rather on the details of the observations and choice of bandpasses for measuring equivalent widths. Hence, we keep them constant throughout this dataset. The exact choice of values is on the basis of Gilbert et al. (2006) Figure 4, as this choice rejects the main locus of MW foreground dwarfs, while only rejecting a small number of giants.

Equation 1 thus defines a membership probability metric that is independent of velocity. Filtering velocity outliers could be warranted because inclusion of a few outlier stars as dSph members that are actually M31 contamination may artificially inflate the velocity dispersion. However, filtering outliers, when they are in fact actually the tails of the dSph member distribution will serve to incorrectly *decrease* the implied dispersion. In the presence of contamination that overlaps in all of our observable parameters, it is thus impossible to completely correct for these effects. Because of this, we adopt a relatively agnostic approach of not using velocities in our membership formulation.

This formulation leads to our adopted definition of “member” stars for the discussion below: those for which $P_{\text{memb}} > 0.1$. As is apparent from the velocity histograms in §4, this choice is conservative in the sense that it excludes some stars that are likely members based on their radial velocities. However, it also means that those that *are* selected as members are generally rather secure members on the basis of all the information available aside from radial velocity. This serves to decrease the aforementioned biases in the kinematical parameters when contamination is small relative to the member population (true in the inner regions for most of the dSph we examine here).

For cross-checking purposes, we considered alternate selection methods. For And I, III, V, VII, IX, X, and XIV, we considered an alternate member selection method based on velocity, spatial proximity, and explicit photometric metallicity estimates (rather than the implicit metallicity dependence based on CMD location described above). We find that the dispersions reported below all agree within 1σ . In addition, for a few dSphs, we compare the likelihood method of Gilbert et al. (2006) (adjusted to the distance of the dSph instead of the M31 mean). We find that the method described above rejects as MW stars nearly the same set of stars as those labeled probable dwarf stars by the Gilbert et al. (2006) likelihood method.

3.3. dSph Kinematical Modeling

With heliocentric radial velocities and spatial and photometric membership probabilities, we are now prepared to describe the kinematics of the dSphs of our sample. We model the velocities of member stars in each dSph as a Gaussian distribution with a systematic velocity μ and dispersion σ . This assumption of Gaussianity would be violated if there is significant contamination from unresolved binaries (e.g., Minor et al. 2010). However, for the galaxies we present with more than two members, a Shapiro-Wilk test (Shapiro & Wilk 1965) reveals that the null hypothesis that the radial velocity distributions are Gaussian cannot be rejected at the $\alpha = 0.05$ level for any of the galaxies. Thus, our assumption of Gaussianity is plausible for these data.

We estimate parameters for the radial velocity distribution using a maximum likelihood estimator similar to that of Kalirai et al. (2010) and Walker et al. (2007), but with a factor that includes our method of assigning membership probabilities. The likelihood we adopt has the form

$$\log L(\sigma, \mu | v_i, \sigma_{t,i}, p_i) = -\frac{1}{2} \sum_{i=1}^N \left[p_i \log(\sigma^2 + \sigma_{t,i}^2) + p_i \frac{(v_i - \mu)^2}{\sigma^2 + \sigma_{t,i}^2} + p_i \log(2\pi) \right] \quad (2)$$

where the p_i s are membership probabilities for each star computed as per Equation 1, and $\sigma_{t,i}$ is the per-star velocity error (including the 2.2 km s^{-1} floor). This likelihood is numerically maximized, the Hessian is computed at this maximum, and inverted to obtain the covariance matrix. We adopt as the error on σ and μ the square root of the diagonal elements of this matrix.

As described in the previous subsection, for the final systemic velocity and velocity dispersion, we only accept stars with membership probabilities $P_{\text{memb}} > 0.1$. We thus filter out all of the stars with a high probability of being non-members, because even with low weights from Equation 2, large outliers strongly bias the parameter estimates. For the same reason, we also reject stars with velocities far from the cold spike for each dwarf (limits determined on a case-by-case basis as detailed in §4). This serves to filter out a small number of MW foreground stars that happen to lie near a satellite spatially and near the fiducial isochrone in the CMD. The precise range of accepted velocities for each satellite are specified

in §4. We emphasize, however, that the ranges selected are significantly broader than the velocity peaks for each satellite, so as not to bias the kinematical parameter estimates.

4. SPLASH M31 DSPHS

With our reduction and analysis procedure outlined in §3.1 and 3.2, we present the full catalog of stars we identify as likely dSph members in Table 2. Non-member stars are available to the reader on request. We also present a summary of the properties of each dSph studied here in Table 3, including our results for systemic velocities and total velocity dispersions. Dwarfs with no reported σ_{LOS} have too few likely members to reliably compute a velocity dispersion.

In the sub-sections that follow, we describe our results and a brief discussion for each satellite in the sample. These each include a Figure showing CMDs, spatial distributions, and velocity histograms of the sample for each dSph. They also describe any deviation from the fiducial parameters described in the previous section for membership selection. We also include a discussion of any relevant previous kinematics for each dSph and compare our results.

4.1. *And I*

And I, originally discovered by van den Bergh (1972), is one of the brightest of M31’s dSph companions ($M_V = -11.8$, $L_V = 4.5 \times 10^6 L_\odot$, similar to the MW dSph Leo I). We present our data for this galaxy in Figure 5. A cold spike is immediately apparent near -400 km s^{-1} in the velocity histogram. However, the tails reveal an unusual aspect of And I that complicate the kinematics: it is embedded within M31’s Giant Southern Stream (GSS, Ibata et al. 2001). The GSS is M31’s largest tidal feature, and as described in Gilbert et al. (2009) and Kalirai et al. (2010), And I lies in the same area on sky as the GSS envelope. The GSS shows significant overlap with And I in kinematics and has some overlap in metallicity, as its properties are closer to that of a dSph than the general halo population. Additionally, And I is one of the closest dSphs to M31 and the overall morphology of the galaxy hints at tidal disruption (e.g., McConnachie & Irwin 2006). Thus the choice of the η parameter in Equation 1 has a significant effect on our derived kinematics, because GSS stars are likely entering into the sample when η is large.

The primary effect is that increasing η serves to more strongly weight stars at larger radii, which have a higher probability of being GSS contaminant stars. We show how this influences our modeling in Figure 6, which plots how our parameter estimates for σ_{LOS} and v_{sys} are affected by the choice of η . The systemic velocity varies slightly but within the error bars of any given measurement, while σ_{LOS} varies significantly for large η . We note, however, that the variation is initially relatively flat, suggesting that at small radii the contamination is not altering the resulting parameters (at least within the error bars). Hence, we choose a value of $\eta = 0.75$, at approximately the value where the upward trend begins. This is significantly more conservative than our fiducial value ($\eta = 1.5$), but serves to down-weight stars in the outskirts of the dSph.

We note that while more conservative in the sense of having fewer stars, our result using the analysis procedure presented here is close to (well within error bars of) the earlier analysis of the same dataset performed in Kalirai et al. (2010). In either case, however, it is difficult to analyze either the effects of tidal stripping or intrinsic radial gradients in the velocity dispersion, given the GSS contamination.

4.2. *And III*

And III is another relatively bright M31 dSph ($M_V = -10.2$, $L_V = 1.0 \times 10^6 L_\odot$), also discovered by van den Bergh (1972). We present our SPLASH results for this satellite in Figure 7. As for And I, a cold spike is clearly present, in this case near -350 km s^{-1} . While near the fringe of the GSS, there is still a hint of possible GSS structure in the form of a slight excess of stars with overlapping velocities far from the center of the satellite. Additionally, there will be a contribution from the tails of the M31 halo distribution given that And III is relatively close to M31 on the sky (5° , or 68 kpc projected). We plot the variation of σ_{LOS} and v_{sys} with η in Figure 8, revealing only a weak dependence, as in And I. However, there is a slight upturn in σ_{LOS} near our fiducial value. Therefore, we adopt $\eta = 0.75$, matching the choice for And I.

Our velocity dispersion for And III here is higher than Kalirai et al. (2010), which found 4.7 ± 1.8 . This is driven in part by the inclusion of a third mask with additional members, and differences in our procedure for determining per-star errors addresses the remainder of the difference. The primary cause, however, is likely the different methods used for determining membership between this work and Kalirai et al. (2010). In particular, the two most extreme velocity members (the highest and lowest velocity members from Figure 7) are included here, and are not in Kalirai et al. (2010), due to their status as outliers. As described in §3.2 and 3.3, such outliers have a significant influence on the kinematical parameter estimates, but because of the overlap between the M31 halo/spheroid distribution and the dSph member populations, it is ambiguous whether or not these stars should actually be included as members. This satellite is the most extreme case in that none of the others have such extreme outliers that otherwise overlap in the membership parameters. Hence, for consistency with the remainder of this paper we keep these stars as members and report the resulting kinematical parameters.

4.3. *And V*

We present our results for And V (discovered by Armandroff et al. 1998) in Figure 9. And V ($M_V = -9.6$, $L_V = 5.9 \times 10^5 L_\odot$) shows a pronounced and very clean cold spike near -400 km s^{-1} , and our kinematic parameter estimates show no significant dependence on η . Because the velocity peak is well away from any contaminants in velocity space, and this dSphs is some distance on the sky from M31 (8.0° , or 110 kpc projected), the membership and parameter estimates are quite secure. Thus, for this dSph, we use our fiducial membership parameters. Additionally, our derived systemic velocity is consistent within error bars of the value adopted in Evans et al. (2000) from the dataset of Guhathakurta et al.

TABLE 2
SPLASH M31 dSPH STARS

Mask ¹	Star ID ²	RA ³	Dec ⁴	T_2 ⁵	$M - T_2$ ⁶	v_{helio} (km/s) ⁷	Na EW ⁸	P_{memb} ⁹
d1.1	1005484	0 ^h 45 ^m 49. ^s 6	+38°11'51''	22.21 ± 0.07	1.67 ± 0.11	−396.1 ± 8.6	2.0 ± 1.3	0.0
d1.1	1005334	0 ^h 45 ^m 51. ^s 7	+38°8'57''	20.73 ± 0.02	1.83 ± 0.03	−381.9 ± 2.2	0.7 ± 0.4	0.007
d1.1	1005398	0 ^h 45 ^m 50. ^s 8	+38°13'44''	20.53 ± 0.02	1.76 ± 0.03	−371.3 ± 3.5	0.3 ± 0.4	0.0
...

NOTE. — This table is available in its entirety in a machine-readable form in the online journal. A portion is shown here for guidance regarding its form and content. Stars not classified as members but with successful radial velocity measurements can be made available upon request to the authors.

¹ Name of the mask on which this star was observed (see Table 1).

² ID number of the star (unique within a dSph field).

³ Right Ascension of the star (J2000).

⁴ Declination number of the star (J2000).

⁵ Washington T_2 magnitude (extinction corrected).

⁶ Washington $M - T_2$ color (extinction corrected).

⁷ Heliocentric radial velocity of this star.

⁸ Equivalent width of Na I λ 8190 feature.

⁹ Membership probability computed following Equation 1.

TABLE 3
SUMMARY OF M31 dSPH PROPERTIES.

Name ¹	RA ²	Dec ³	M_V ⁴	d_{LOS} ⁵	r_{M31} ⁶	N_{memb} ⁷	v_{sys} ⁸	σ_{LOS} ⁹	Sources ¹⁰
And I	00:45:39.800	+38:02:28.00	−11.8 ^{+1.0} _{−1.0}	744.7 ^{+24.4} _{−23.6}	58.4 ^{+35.4} _{−34.3}	51	−376.3 ± 2.2*	10.2 ± 1.9*	a,b,c
And III	00:35:33.800	+36:29:52.00	−10.2 ^{+0.3} _{−0.3}	748.2 ^{+24.5} _{−23.7}	75.2 ^{+35.5} _{−34.4}	62	−344.3 ± 1.7*	9.3 ± 1.4*	a,c,d
And V	01:10:17.100	+47:37:41.00	−9.6 ^{+0.3} _{−0.3}	820.4 ^{+15.3} _{−15.0}	118.2 ^{+29.9} _{−29.0}	85	−397.3 ± 1.5	10.5 ± 1.1	a,e,f
And VII	23:26:31.700	+50:40:33.00	−13.3 ^{+0.3} _{−0.3}	762.1 ^{+25.0} _{−24.2}	218.3 ^{+35.8} _{−34.7}	136	−307.2 ± 1.3	13.0 ± 1.0	a,c,g
And IX	00:52:53.000	+43:11:45.00	−8.1 ^{+0.4} _{−0.1}	765.6 ^{+25.1} _{−24.3}	40.5 ^{+35.9} _{−34.7}	32	−209.4 ± 2.5	10.9 ± 2.0	a,c,h
And X	01:06:33.700	+44:48:16.00	−7.4 ^{+0.1} _{−0.1}	701.5 ^{+33.1} _{−31.6}	109.4 ^{+41.9} _{−40.2}	27	−164.1 ± 1.7	6.4 ± 1.4	a,i
And XI	00:46:20.000	+33:48:05.00	−6.9 ^{+0.5} _{−0.1}	871.0 ^{+84.0} _{−76.6}	139.1 ^{+87.9} _{−80.6}	2	−461.8 ± 3.7**	...	a,j
And XII	00:47:27.000	+34:22:29.00	−6.4 ^{+0.5} _{−0.1}	831.8 ^{+44.7} _{−44.7}	109.2 ^{+53.8} _{−51.2}	2	−525.3 ± 3.4**	...	a,j,k
And XIII	00:51:51.000	+33:00:16.00	−6.7 ^{+0.4} _{−0.1}	871.0 ^{+84.0} _{−76.6}	150.0 ^{+87.9} _{−80.6}	12	−185.4 ± 2.4	5.8 ± 2.0	a,j
And XIV	00:51:35.000	+29:41:49.00	−8.5 ^{+0.1} _{−0.1}	734.5 ^{+120.6} _{−103.6}	162.3 ^{+123.3} _{−106.5}	48	−480.6 ± 1.2	5.3 ± 1.0	a,l
And XV	01:14:18.700	+38:07:03.00	−9.8 ^{+0.4} _{−0.4}	770.0 ^{+70.0} _{−70.0}	93.6 ^{+74.6} _{−74.3}	29	−323.0 ± 1.4	4.0 ± 1.4	a,m,n
And XVI	00:59:29.800	+32:22:36.00	−9.2 ^{+0.5} _{−0.5}	525.0 ^{+50.0} _{−50.0}	279.4 ^{+56.2} _{−55.8}	7	−367.3 ± 2.8	3.8 ± 2.9	a,m,n
And XVIII	00:02:14.500	+45:05:20.00	−9.7 ^{+0.1} _{−0.1}	1355.2 ^{+83.6} _{−78.8}	590.9 ^{+82.6} _{−82.6}	22	−332.1 ± 2.7	9.7 ± 2.3	a,o
And XXI	23:54:47.700	+42:28:15.00	−9.3 ^{+0.1} _{−0.1}	859.0 ^{+51.0} _{−51.0}	149.2 ^{+57.1} _{−56.7}	6	−361.4 ± 5.8	7.2 ± 5.5	a,p
And XXII	01:27:40.000	+28:05:25.00	−6.2 ^{+0.1} _{−0.1}	794.0 ^{+239.0} _{−239.0}	220.6 ^{+240.4} _{−240.3}	7	−126.8 ± 3.1†	3.54 ^{+4.16†} _{−2.49}	a,p

REFERENCES. — a. Brasseur et al. (2011), b. Paturel et al. (2000), c. McConnachie et al. (2005b), d. Karachentseva & Karachentsev (1998), e. Armandroff et al. (1998), f. Mancone & Sarajedini (2008), g. Karachentsev et al. (2001), h. Zucker et al. (2004), i. Zucker et al. (2007), j. Martin et al. (2006), k. Chapman et al. (2007), l. Majewski et al. (2007), m. Ibata et al. (2007), n. Letarte et al. (2009), o. McConnachie et al. (2008), p. Martin et al. (2009)

¹ Name of the dSph.

² Right Ascension of the dSph.

³ Declination of the dSph.

⁴ V-band absolute magnitude of the dSph.

⁵ Heliocentric line-of-sight distance to the dSph in kpc.

⁶ Distance from M31 to the dSph in kpc.

⁷ Number of successful spectra with $P_{\text{memb}} > 0.1$, i.e., dSph member stars.

⁸ Systemic velocity of the dSph estimated according to §3.3 in km s^{−1}.

⁹ Total velocity dispersion of the dSph estimated according to §3.3 in km s^{−1}.

¹⁰ Sources for location, distance, size, and luminosity of the dSph.

* Kinematics for these satellites may be moderately affected by contamination due to M31 substructure – see subsection for details.

** These measurements depend on an uncertain detection of a cold spike – see subsection for details.

† The parameter estimates for this object is based on a different method than the other dSphs – see subsection for details.

And I

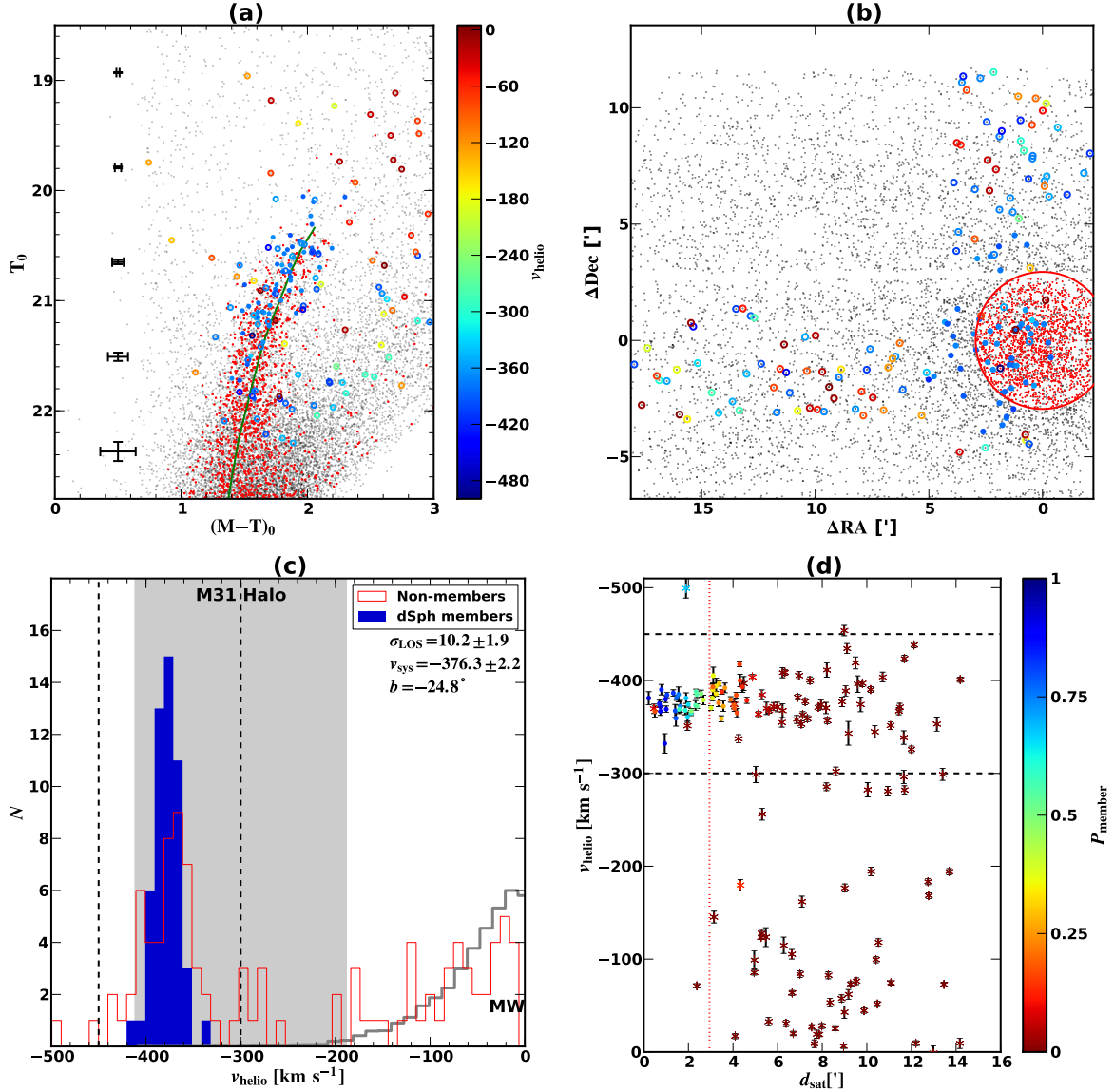


FIG. 5.— SPLASH results for And I. Panel (a) shows the (Galactic extinction corrected) color-magnitude diagram for And I, and panel (b) shows the spatial distribution of the same objects. R_{eff} for the galaxy is indicated in (b) as the large red circle. In both panels, circles are objects with spectra and measured radial velocities. Filled circles are those identified as members according to the criteria discussed in §3.2, open circles are non-members, and the color code gives the heliocentric radial velocity. Small points are stellar-like objects detected photometrically, but without spectra. The red points are those that lie inside R_{eff} and satisfy the DDO51 pre-selection criteria indicating a high likelihood of being a red giant, while the black points are the remainder. The (green) line passing through these points in panel (a) is the adopted isochrone. Panel (c) shows the heliocentric radial velocities of all spectra from the And I mask with sufficient signal-to-noise to measure a velocity as the open (red) histogram. The filled (blue) histogram is for members. Also shown is a grey shaded region indicating the center and 1σ width of the M31 halo velocity distributions, as characterized by Chapman et al. (2006). Versions of this figure for other dSph farther than 100 kpc (projected) do not show this halo distribution, as the typical number of halo stars per mask is very low at those distances. Also shown as a (grey) histogram near $v_{\text{helio}} = 0$ is an arbitrarily normalized distribution of MW foreground stars derived from the Robin et al. (2003) model in the direction of And I, based on a CMD selection box approximately matched to panel (a). Panel (d) shows v_{helio} of all stars with successfully recovered velocities as a function of their distance from the center of the satellite, with error bars derived following the procedure described by §3.1. Circles are classified as members and star-shaped symbols are non-members, with the color code signifying the membership probability. The dotted (red) vertical line is R_{eff} for And I. The dashed (black) vertical lines in both (c) and (d) indicate the minimum and maximum velocities for inclusion as a member.

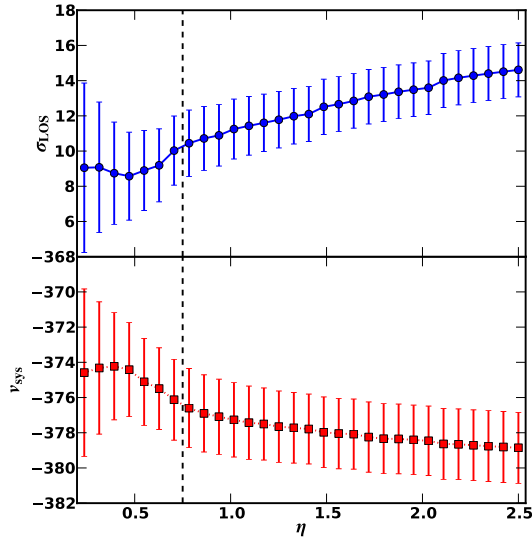


FIG. 6.— Dependence of kinematical parameter estimates on And I membership parameter η . η is defined as the free parameter of Equation 1 that defines the scale relative to R_{eff} outside which membership probabilities fall off. The upper panel (blue) displays the effect of η on the inferred velocity dispersion, while the lower (red) is for the systemic velocity. In both cases the values and associated error bars are derived for each η following the procedure described in §3.3. The vertical dashed (black) line is the η value adopted for And I.

(2000).

We also note the presence of another possible cold spike in this field at ~ -70 km s $^{-1}$. At such low heliocentric velocity, this feature is likely to be associated with the MW, particularly given the low galactic latitude of And V ($b = -15.1^\circ$). One possible candidate may be the Monoceros ring feature (Newberg et al. 2002), as this overdensity has been noted in fields near M31 (Ibata et al. 2003). The cold feature in Figure 9 has a radial velocity consistent with extrapolation of the the velocity-Galactic longitude relation for the Monoceros ring (Crane et al. 2003, Figure 2), but it is not clear that the Mon should have a high density in this field. Alternatively, the cold spike may be related to the Triangulum-Andromeda feature (described in more detail in §4.5), but it is not at the expected radial velocity ($v_{\text{helio}} \sim -130$ km s $^{-1}$ for this field, Rocha-Pinto et al. 2004). However, a detailed analysis of the source of this feature is beyond the scope of this paper.

4.4. And VII

And VII, discovered by Karachentsev & Karachentseva (1999), is the brightest of M31’s dSph companions, at $M_V = -13.3$, $L_V = 1.8 \times 10^7 L_\odot$ (although M31’s dE satellites are only 1-2 mags brighter). We present our results in Figure 10. A cold spike is immediately apparent near -300 km s $^{-1}$. While this velocity is close to that of the peak of the M31 halo, And VII has a very large projected distance from M31 (16.2° , or 220 kpc projected), and hence M31 halo contamination is likely negligible for this galaxy. Additionally, as is apparent from Figure 11, our recovered kinematical parameters are nearly independent of η , motivating our choice of $\eta = 3$. Because this dSph is so bright, the red giant branch is very well populated, the tails of the metallicity distribution are well populated, and we thus increase our isochrone color

width $\sigma_c = 0.25$. Hence, most of our spectra for these masks are classified as likely members, even well beyond the half-light radius, and these stars cluster tightly in the cold peak. This further underscores the reliability of our DDO51 pre-selection’s ability to select giants over dwarfs when there are enough giants available. Additionally, our recovered v_{sys} is almost identical to that of Evans et al. (2000) and Guhathakurta et al. (2000).

4.5. And IX

And IX, discovered by Zucker et al. (2004), is one of the fainter M31 dSph we consider here ($M_V = -8.1$, $L_V = 1.5 \times 10^5 L_\odot$). We present our observations in Figure 12. A cold spike is present near -200 km s $^{-1}$, but the velocity histogram also shows spikes near -330 and -130 km s $^{-1}$. The former is consistent with M31 halo contamination, strong in this field because And IX is quite close to M31 (2.7° , or 37 kpc projected). The latter cold spike, however, is far from the expected peak for M31, while the MW distribution for red stars in this field peaks at -20 km s $^{-1}$ (Robin et al. 2003). Instead, a plausible explanation for this peak is the Triangulum-Andromeda (TriAnd) overdensity (Rocha-Pinto et al. 2004). And IX lies near a high density region of TriAnd feature, and given the inhomogeneity of the TriAnd feature, a significant TriAnd population in this field is quite plausible. Additionally, this peak is fully consistent with the systemic velocity and width of TriAnd (Rocha-Pinto et al. 2004, Figure 4; And IX is at $l = 123$ and $v_{\text{helio}} = -130$ implies $v_{\text{gsr}} = 46$ km s $^{-1}$ for And IX). Additionally, both this feature and the peak at -330 km s $^{-1}$ are uniformly spread across the field, while stars near -200 km s $^{-1}$ are spatially concentrated at the photometric center of the satellite.

Thus, we take the peak at -200 km s $^{-1}$ as the peak for And IX, consistent with the results of Chapman et al. (2005). While our membership criteria eliminate most stars in the other two peaks, a small number of outliers nevertheless pass our membership cuts (while no starlist is published in Chapman et al. 2005, this likely includes the outlier mentioned based on the distance given in that work). Thus, for this satellite, we impose more stringent final velocity restrictions (vertical dashed lines in Figure 12) to filter out these extreme outliers, as they are consistent with falling within the distributions of properties for the other populations. We note that kinematic results we obtain with this procedure differ at the $1 - 2\sigma$ level from Chapman et al. (2005) and Collins et al. (2010), although our sample has roughly twice the number of member stars.

4.6. And X

Our results for And X (discovered by Zucker et al. 2007, $M_V = -7.4$, $L_V = 7.5 \times 10^4 L_\odot$) are shown in Figure 13. A clear cold spike is apparent near -165 km s $^{-1}$. This field is significantly farther from the center of M31 relative to And IX (5.6° , or 77 kpc projected), and hence the M31 halo contamination is much lower, so we use our fiducial parameters, as changing η does not affect our kinematical results. We note that the dispersion we find here is 1.4σ from the result of Kalirai et al. (2009) using the same observations, due to the fact that our method does not formally reject all of the velocity outliers men-

And III

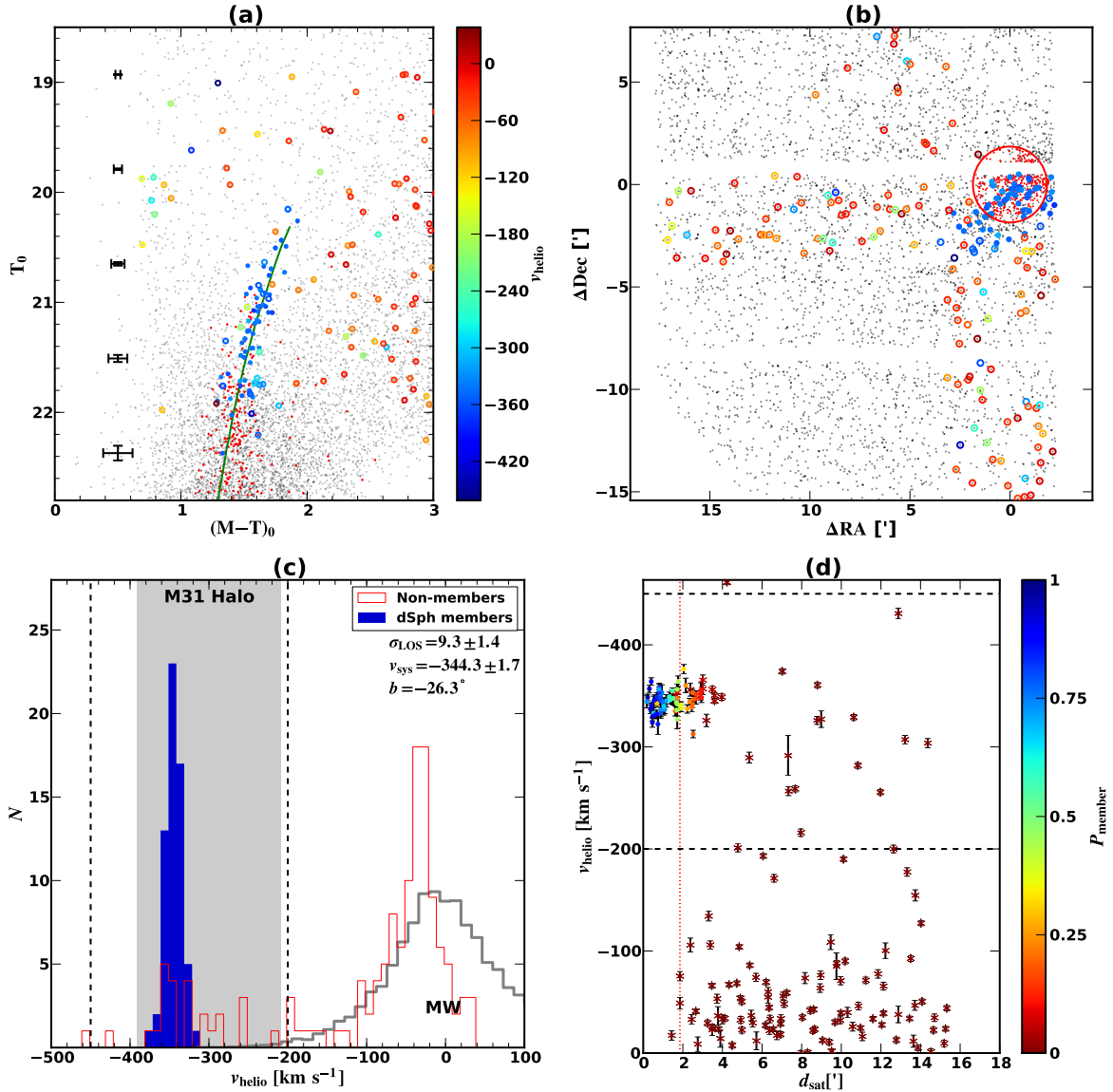


FIG. 7.— Same as Figure 5, but for And III.

tioned in Kalirai et al. (2009). If we reject outlier stars in the same fashion, we reproduce a very similar sample as that paper and nearly identical kinematic results.

We also note the presence of another peak in the histogram well offset from the MW expectation at ~ -80 km s $^{-1}$, and a possible smaller peak at ~ -130 km s $^{-1}$. This field is in a relatively high density portion of the TriAnd feature, and the kinematics of Rocha-Pinto et al. (2004) suggest this latter peak is due to this feature. However, the broader ~ -80 km s $^{-1}$ is well offset from the expected velocity for this feature, suggesting either TriAnd has a wider velocity dispersion than previously though, or this peak is a different (most likely MW) substructure.

4.7. And XI

Our spectroscopy for And XI (discovered by Martin et al. 2006) is shown in Figure 14. And XI is one of

the faintest dSphs in our sample ($M_V = -6.9$, $L_V = 4.9 \times 10^4 L_\odot$), and the field is both small and has few bright RGB candidates. Hence, we do not see an obvious cold spike. We do obtain spectra of two stars near the center of the dwarf that have very close radial velocities. The large distance from M31 (7.5° , or 102 kpc projected) combined with their proximity to each other and the center of the dSph renders it plausible that these are dSph members rather than M31 halo stars. Our reported v_{sys} is derived assuming these two are members. However, this result is in conflict with Collins et al. (2010), which report five stars near -420 km s $^{-1}$. Thus, while we report the mean velocity of these two stars, it is quite possible these are simple M31 contaminants and we have detected no actual members.

4.8. And XII

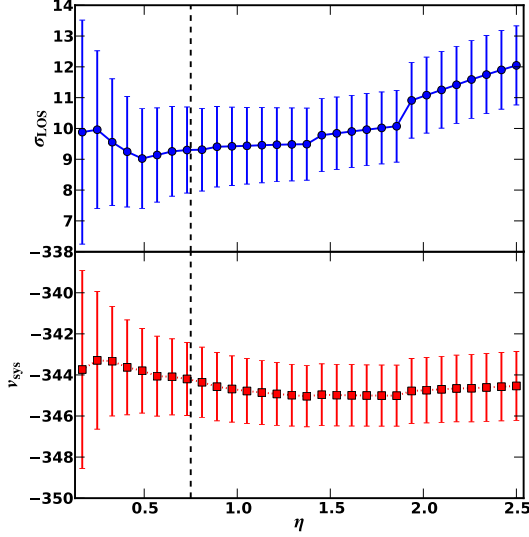


FIG. 8.— Same as Figure 6, but for And III.

Our spectroscopy for And XII (discovered by Martin et al. 2006) is shown in Figure 15. As with And XI, this field is very sparse due to the faintness of the satellite ($M_V = -6.4$, $L_V = 3.1 \times 10^4 L_\odot$) and distance from M31 (7.0° , or 95 kpc projected). We see no clear cold spike, but there are two stars that lie at much more negative velocities than expected for the M31 halo. As with And XI, we report the mean of these two as v_{sys} , and again, this is offset from Collins et al. (2010) by $\sim 30 \text{ km s}^{-1}$, so these v_{sys} come with the caveat that they may well be non-detections.

4.9. And XIII

Our spectroscopy for And XIII (discovered by Martin et al. 2006), another faint dSph ($M_V = -6.7$, $L_V = 4.1 \times 10^4 L_\odot$) is shown in Figure 16. We adopt all fiducial parameters for this dwarf, and see a cold spike of 12 stars that pass membership cuts near -200 km s^{-1} . The vertical dashed lines in the velocity histogram clearly indicate that we have explicitly cut out stars not near the cold spike, which may at first appear to artificially shrink the dispersion. However, this actually only serves to eliminate two stars (all others failed the membership cuts with the fiducial parameter choices). One of these stars is far removed from the dSph in all three diagrams, and hence is likely an M31 contaminant. The other star removed from by the cut, has $v_{\text{helio}} = -221 \text{ km s}^{-1}$ and is very close to the And XIII isochrone, as well as lying within the half-light radius. However, it is also the faintest star in this spectroscopic sample, with a $S/N = 1.9$. Hence, only a single CaT line is detected in the spectrum, and may be biased by nearby sky lines. We therefore reject that particular star and compute the kinematic parameters from the more well-defined cold spike. The resulting parameters are roughly 1σ discrepant from the Collins et al. (2010) result, but we note that our sample is 4 times larger, and hence likely more robust.

This field also includes a relatively large number of non-members, despite its large distance from M31 (8.5° , or 116 kpc projected) and relatively large Galactic latitude ($b = -29^\circ$). Most of this structure is uniform across

the field, suggesting that it is either foreground or large-scale halo structure. In particular, there is a hint of a peak at $\sim -130 \text{ km s}^{-1}$, which is consistent with the expected velocities for the TriAnd feature in this field. The stars with radial velocities in the -500 to -300 km s^{-1} range are very unlikely to be of MW origin, however. The distance from M31, assuming the halo model of Guhathakurta et al. (2005), implies the number of M31 RGB stars present in this field is higher than expected, suggesting that the environs of And XIII include some sort of overdensity of M31 stars. Whether this is due to substructure in M31’s halo, tidal stripping of other satellites, or a connection to M33 (And XIII lies roughly along the M31-M33 axis), or simply statistical coincidence, are questions beyond the scope of this paper.

4.10. And XIV

And XIV (discovered by Majewski et al. 2007, $M_V = -8.5$, $L_V = 2.1 \times 10^5 L_\odot$), is unusual because of its large velocity relative to M31. This may imply it is unbound or barely bound to M31, further supported by its large on-sky distance from M31 (11.7° , or 160 kpc projected). Because of this isolation, it shows a clean cold peak, immediately apparent in Figure 17 near -480 km s^{-1} . We note that our results here are fully consistent with Majewski et al. (2007), although this should come as no surprise given that 2 of our 3 masks are from the same dataset.

4.11. And XV

And XV (discovered by Ibata et al. 2007), is a reasonably bright ($M_V = -9.8$, $L_V = 7.1 \times 10^5 L_\odot$), relatively isolated dSph (6.8° , or 93 kpc projected). Hence, Figure 18 has a readily apparent cold spike near -300 km s^{-1} . However, caution is warranted for this dSph, as it is clear that a significant number of stars in the cold spike do not pass our membership criteria. Examining the spatial diagram demonstrates clearly that there are stars with velocities consistent with the cold spike that are many R_{eff} away from the galaxy center. While the velocities of these stars are near that of the M31 halo distribution, some appear to be kinematically nearly as cold as the satellite itself, and lie along the dSph locus in the CMD. This suggests these stars have been tidally stripped from And XV, a conclusion further supported by the dSph’s disturbed morphology (Ibata et al. 2007). Other stars near that velocity are far from the dSph in the CMD, however. These may be stars from the “Stream B” feature of the M31 halo that lies near And XV and has very similar kinematics (Chapman et al. 2008).

Given the presence of these contaminants, it is clear that the choice of η will influence our kinematical results. This is apparent from Figure 19, where the sudden jumps in σ_{LOS} and increasing trend towards larger η indicates the effect of contaminants. Fortunately, for $\eta \lesssim 1.3$, the kinematical parameter estimates are constant (well within the error bars). Hence, we use $\eta = 1.3$ for this dSph. Additionally, we have adopted a value of $\sigma_c = 0.2$ to account for a somewhat wider CMD for this object (although we note that we obtain similar kinematical parameters if we use our fiducial $\sigma_c = 0.1$). Our resulting σ_{LOS} and v_{sys} are $1 - 2\sigma$ discrepant from Letarte et al. (2009), however. This is likely due to a combination of

And V

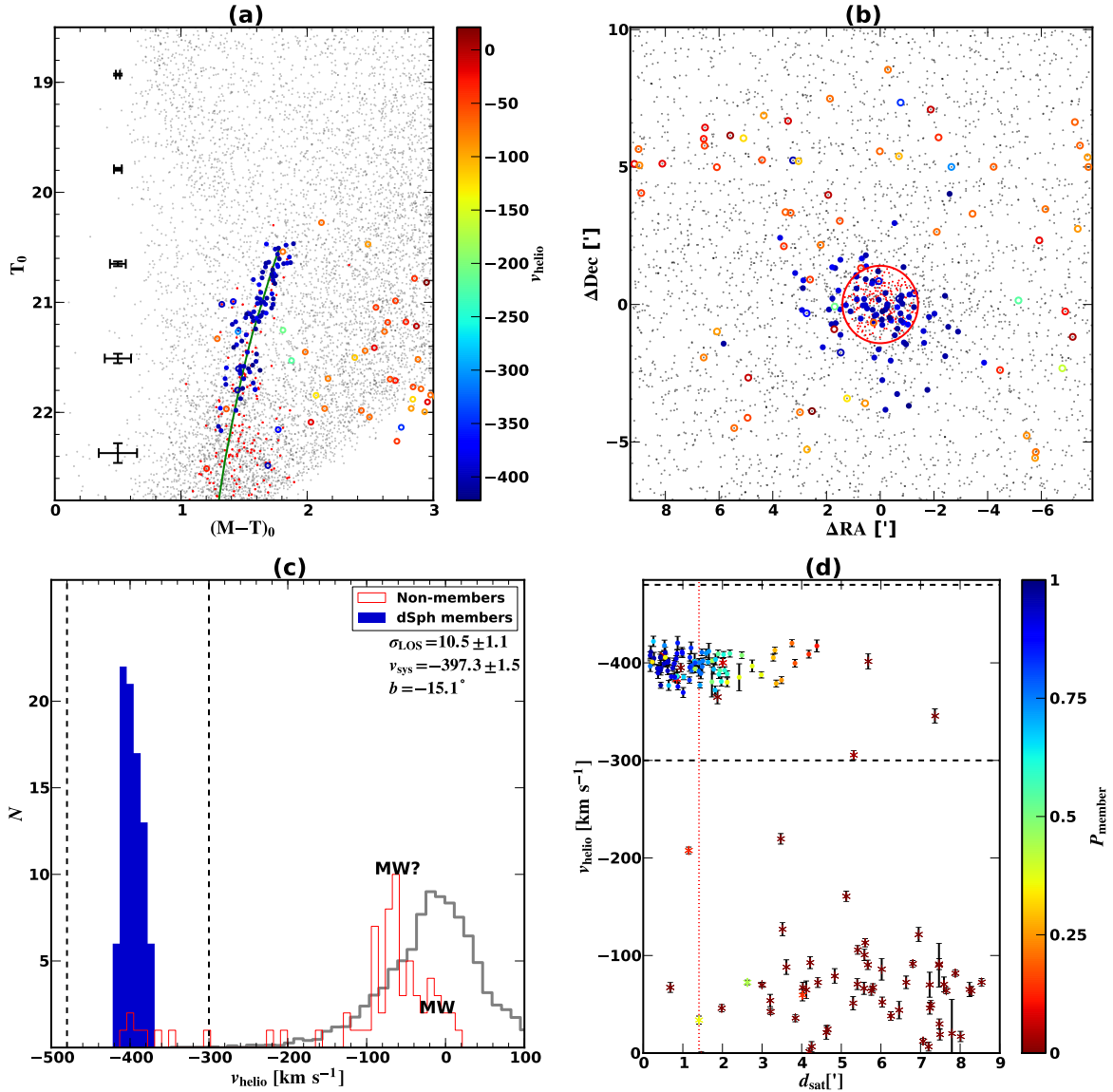


FIG. 9.— Same as Figure 5, but for And V.

sample size (our sample is 2-3x larger), star-by-star errors (ours are smaller due to use of a higher resolution grating), and our use of a sample that is more strongly weighted towards the center of the dSph. Given the contamination issues outlined above, the stars closest to the center are likely of great importance.

4.12. And XVI

Our And XVI (discovered by Ibata et al. 2007, $M_V = -9.2$, $L_V = 4.1 \times 10^5 L_\odot$) field is rather sparse in successful targets, but Figure 20 does show a centrally-concentrated cluster of stars near -360 km s^{-1} . Fortunately, And XVI's relatively large distance from M31 (9.5° , or 130 kpc projected) and high galactic latitude ($b = -30^\circ$) implies very little contamination. Our fiducial parameters result in a marginally resolved velocity dispersion. The small number of stars (7) imply that this measurement should be taken with caution, however, as

excluding a few stars from the analysis typically results in a dispersion formally consistent with zero. We note that our v_{sys} is discrepant from Letarte et al. (2009) at the $\sim 3\sigma$ level, however, even when a dispersion is not resolved.

4.13. And XVIII

And XVIII was discovered by McConnachie et al. (2008) and is remarkable in its large line-of-sight distance that formally places it well outside of the M31 system and in fact at the outskirts of the LG. It is also fairly bright ($M_V = -9.7$, $L_V = 6.3 \times 10^5 L_\odot$), and reasonably far from M31 on the sky (8.3° , or 113 kpc projected) and therefore contamination from the M31 halo will likely be small. We present our results for And XVIII in Figure 21, which shows a clear cold spike near -330 km s^{-1} . These stars are centrally concentrated and far from the typical M31 halo star on the CMD. Hence, we conclude

And VII

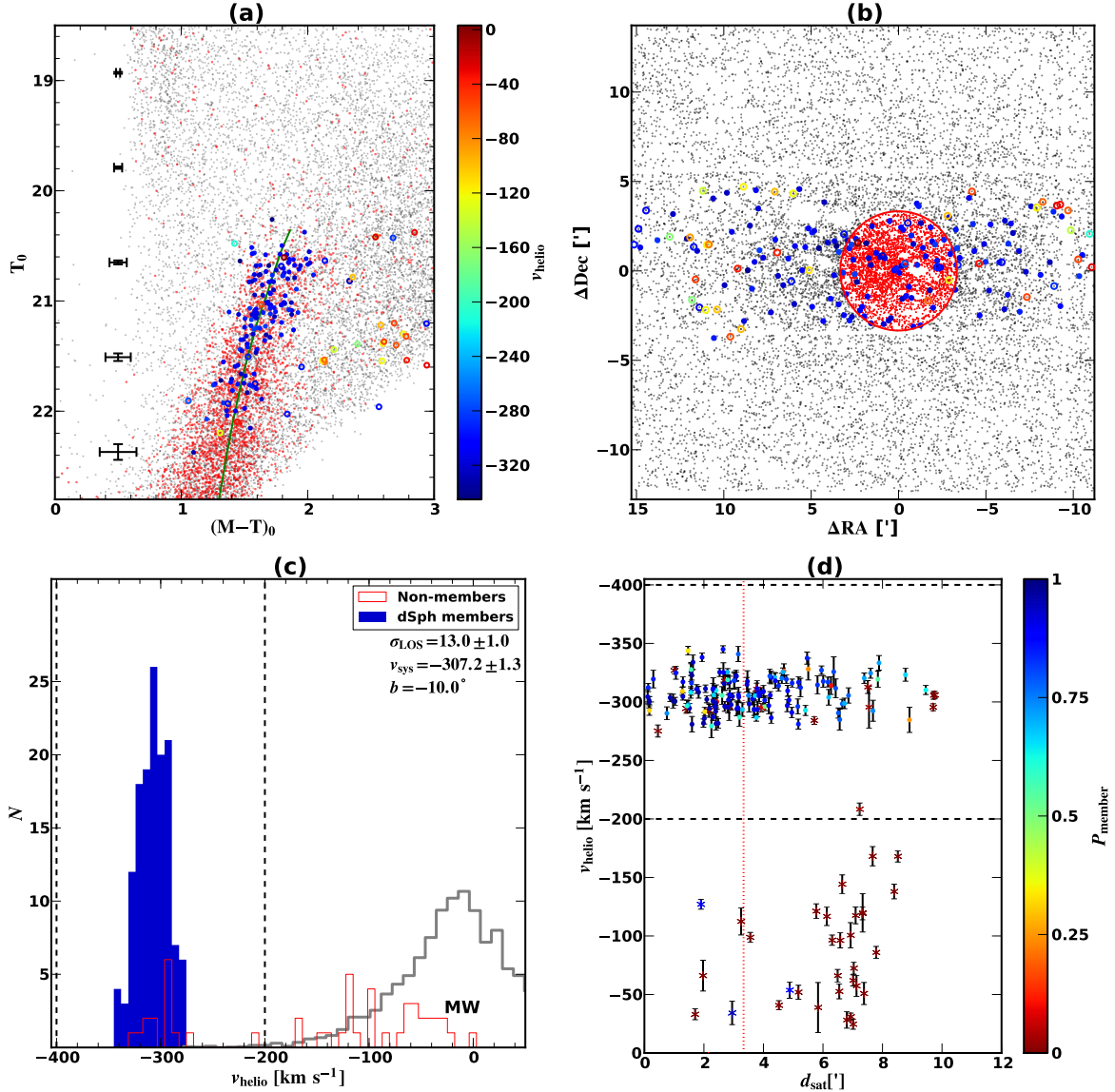


FIG. 10.— Same as Figure 5, but for And VII.

that these observations (the first spectroscopic observations of And XVIII) definitively confirm it as a kinematically cold satellite galaxy. We adopt a $\sigma_c = 0.3$ to accept the wider-than typical CMD (primarily due to relatively shallow targeting photometry).

The v_{sys} we measure is very close to M31's v_{sys} . This is a remarkable coincidence if And XVIII is actually 600 kpc distance from M31 and never interacted. Hence, And XVIII is near its apocenter (and thus nearly at rest relative to M31), and/or closer to M31 (as suggested by our photometry, Beaton et al., in prep.).

4.14. And XXI

And XXI was recently discovered as part of the PAndAS survey, and is relatively luminous ($M_V = -9.3$, $L_V = 4.6 \times 10^5 L_\odot$) but has an atypically large half-light radius/low surface brightness (Martin et al. 2009). It is also quite far from M31 (9.0° , or 123 kpc projected), and

hence contamination from the M31 halo is quite low. We present the first spectroscopic observations of And XXI in Figure 22. The field is sparse, but there is a definite overdensity of stars with radial velocities near -360 km s^{-1} .

For membership criteria, we adopt a larger-than-fiducial $\sigma_c = 0.3$ to account for the relatively shallow T exposure. This mainly serves to include the star near $M - T \sim 1$ (the faintest in the spectroscopic sample), as that star is very near the center of the dSph and hence is plausibly a member. We also note that the brightest star in the member sample is near (and possibly beyond) the expected tip of the red giant branch for this satellite (Martin et al. 2009). It is also the most distant from the center of the dSph in our sample, hence rendering its membership questionable. It is formally included following our method here, but removing it from our sample results in changes to our kinematic parameters that are

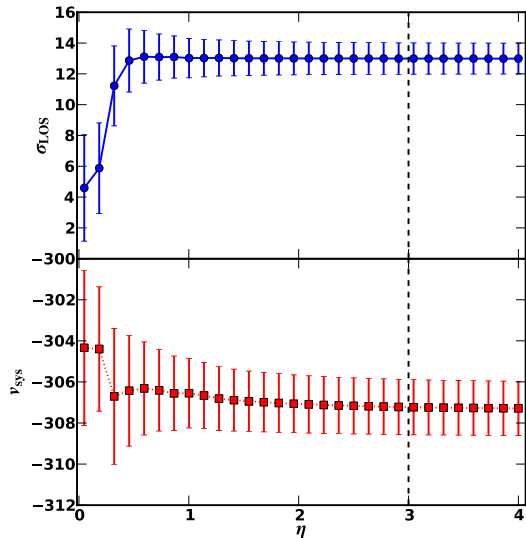


FIG. 11.— Similar as Figure 6, but for And VII. The x-axis has been expanded relative to Figure 6.

well within errors.

With this sample, we find a velocity dispersion with large errors but formally inconsistent (at 1σ) with zero. Additionally, given the clear clustering in radial velocity of four of the stars near the identified RGB of Martin et al. (2009), we consider our data to be spectroscopic confirmation that And XXI is a kinematically cold satellite with $v_{\text{sys}} \approx -363$, although our derived velocity dispersion has large error bars that may be underestimated due to the small sample of only 6 stars.

4.15. And XXII

And XXII, also discovered by Martin et al. (2009), is one of the faintest of the M31 dSphs ($M_V = -6.2$, $L_V = 2.6 \times 10^4 L_\odot$). In Figure 23 we present our results for And XXII. While our success rate at selecting members for spectroscopy was lower for this satellite than others due to a lack of DDO51 pre-selection and the faintness of this galaxy, we do find a concentration of stars within R_{eff} that are kinematically cold. These stars lie along a well-defined sequence that matches the CMD of Martin et al. (2009), and the kinematically cold sample shows an elliptical distribution consistent with the photometric measurements (and ellipticity was *not* included in the target selection). Thus, we spectroscopically confirm a cold population consistent with the hypothesis that And XXII is a bound dSph.

Unlike the other dSphs in this survey, the small number of identified member stars for this dSph results in a likelihood distribution of our velocity dispersion parameter estimate that is clearly non-Gaussian. Hence, our maximum likelihood technique breaks down, because the assumption of normality near the maximum of the likelihood function is invalid. Thus, for this galaxy, we estimate σ and v_{sys} using a Markov chain Monte Carlo (MCMC) method with uniform priors on both parameters (Bradford et al. 2011). We have confirmed that the MCMC reproduces the same results as the ML method in the case of Gaussian distribution. We quote the MCMC results in Table 3.

This dSph is also much closer in projected distance to

M33 than it is to M31: 2.9° and 16.1° to M33 and M31, respectively. This leads to the suggestion that And XXII may be a satellite of M33 rather than M31 (Martin et al. 2009). On the other hand, the line-of-sight distance is closer to M31 than M33, resulting in 3D distances of 130 and 220 kpc, respectively. Adopting an assumption for the total mass of M31 and M33 based on Λ CDM expectations (Guo et al. 2010, Table 1), the Jacobi tidal radius (Binney & Tremaine 2008) of M33 (assuming it is in a circular orbit around M31) is 67 kpc, suggesting that And XXII cannot be bound to M33.

However, our measurements show that And XXII is significantly closer in systemic velocity $v_{\text{sys}} \approx -127$ km s^{-1} to M33 (-180 km s^{-1} , e.g. Huchra et al. 1999) than to M31 (~ -300 km s^{-1}). Experiments with the Via Lactea 2 N-body simulation (Diemand et al. 2008) suggest that line-of-sight velocities this close for two random subhalos like those M33 and And XXII might inhabit are very unlikely. Furthermore, the line-of-sight distance to And XXII is based on tip of the red giant branch distance measurements (Martin et al. 2009). The And XXII RGB is sparsely populated, and hence mis-identifying even a few RGB stars near the tip as dSph stars when they are actually M31 halo field stars would bias the distance closer. There is thus a possibility of substantial changes in the TRGB-determined distance with refined stellar membership (e.g., Letarte et al. 2009), in the sense that corrections are likely to push it closer to M33. If this is indeed the case, our finding that it is also closer in line-of-sight velocity strongly suggests that And XXII is a satellite of M33 rather than M31. In this case, if M33 is taken to be a satellite of M31, as is plausible in a Λ CDM context (Tollerud et al. 2011a), And XXII may be the first detection of a large mass ratio satellite-of-satellite (or sub-subhalo).

5. SCALING RELATIONS OF M31 DSPHS

With velocity dispersions for most of our sample and structural parameters from a variety of previous studies (see Table 3), we are now in a position to consider where M31 dSphs lie on established galaxy scaling relations. To this end, we consider the scaling relations between mass, luminosity, and size for these satellites. In what follows, we do not include And XI, XII, or XXII in our sample due to the aforementioned problems estimating their velocity dispersions.

More specifically, we examine the MRL parameter space explored by Tollerud et al. (2011b). This parameter space consists of deprojected (3D) half-light radius ($r_{1/2}$), the mass within that radius ($M_{1/2}$), and the half-luminosity ($L_{1/2}$). $L_{1/2}$ is straightforward as simply half the observed luminosity of the galaxy. $M_{1/2}$ and $r_{1/2}$ are derived from σ_{LOS} and R_{eff} following the prescriptions of Wolf et al. (2010): $M_{1/2} = 3\sigma_{\text{LOS}}^2 r_{1/2} G^{-1}$. $r_{1/2}$ is a simple scaling of R_{eff} , at least for light profiles like those of the dSphs we study here: $r_{1/2} = 1.315 R_{\text{eff}}$. $M_{1/2}$ is computed using a standard dynamical mass estimator scaled, crucially, to be the mass within $r_{1/2}$, and is *insensitive* to the velocity anisotropy. This only holds in the case of a relatively flat velocity dispersion profile, but the dSphs in our data set satisfy that requirement within the error bars (aside from possibly And I and And III - see §4.1 and 4.2). It is important to note, however,

And IX

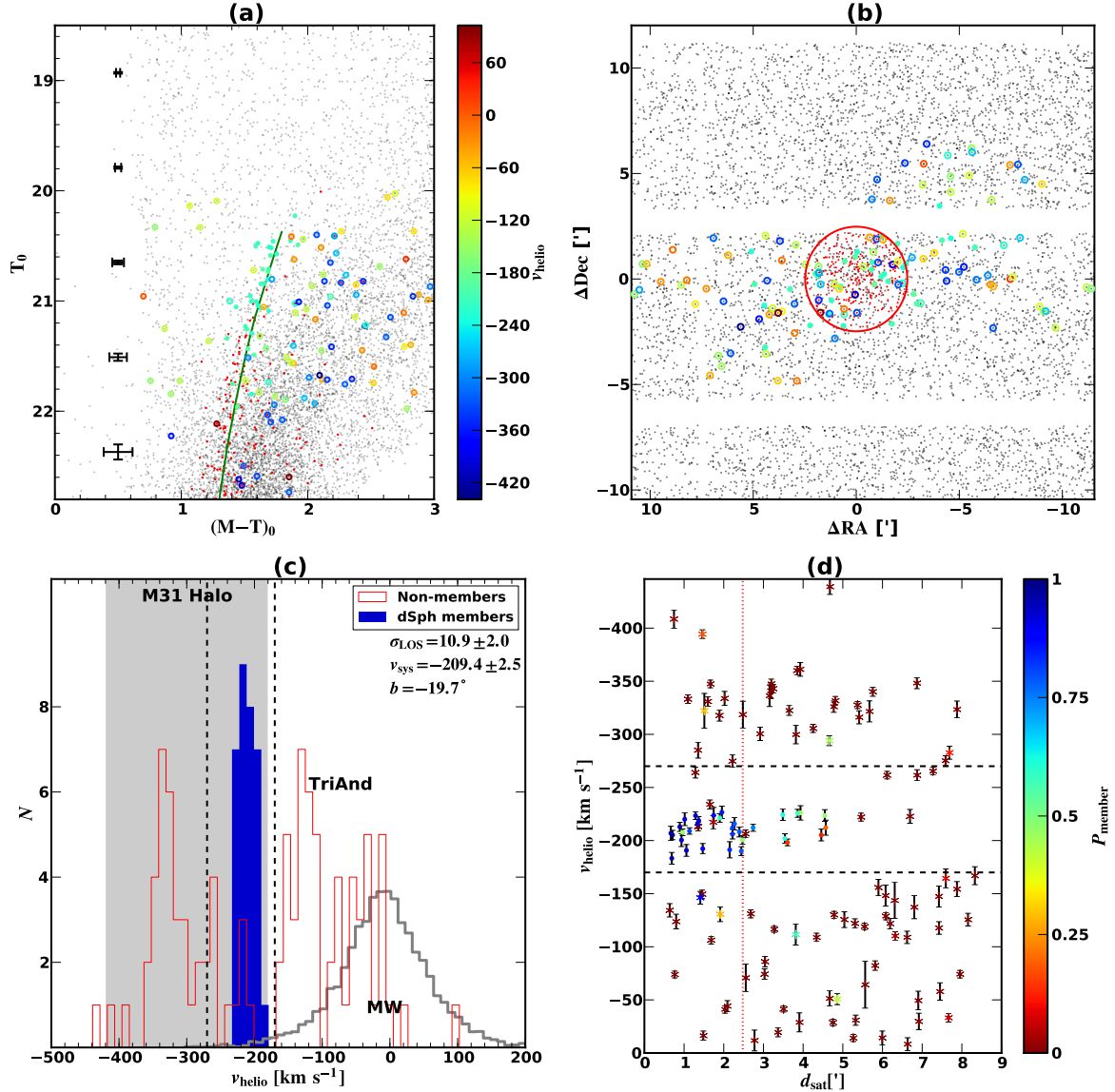


FIG. 12.— Same as Figure 5, but for And IX.

that because $M_{1/2}$ is derived from the velocity dispersion, any systematic errors in the velocity dispersion driven by our method of assigning membership to stars will present themselves in these scalings as errors in $M_{1/2}$.

These scaling relations are also a valuable means to compare M31 dSphs to MW satellites. We use the MW dSph compilation of Wolf et al. (2010), with updates for Boötes I and Segue 1 from Koposov et al. (2011) and Simon et al. (2011), respectively. We present the three projections of the MRL space in Figure 24, with our M31 dSphs as squares (blue) and MW dSphs as triangles (red). In the L - R plane (upper panel), we also plot detection limits for the PAndAS survey (dashed blue, Brasseur et al. 2011) and SDSS (dotted red, Tollerud et al. 2008). To do a proper comparison, MW dSphs that could be detected around M31 should be compared to the true M31 satellites, so we denote MW satellites within the detection limit by filled triangles, and those

that could not be detected around M31 as open triangles.

A careful probabilistic M31/MW comparison for the L - R space (upper panel of Figure 24) has already been performed by Brasseur et al. (2011), and they conclude that there is no significant evidence that the distributions differ between the MW and M31 dSphs. In the lower panels of Figure 24, we see similar levels of scatter as in the upper panel, suggesting there is no significant deviation. We generate 100 Monte Carlo samples of the data in each of the three planes, where each resample is generated by assuming Gaussian distributions for both M31 and the MW data points. We then perform a linear fit, compute the slope and intercept for each resample, and compare the resulting slope/intercept distributions. For both the M - R and M - L planes, we find the M31 and MW distributions to be in accord at $< 1\sigma$, while for L - R there is a slight disagreement of $\sim 1.5\sigma$. Brasseur et al. (2011) find closer agreement with a larger sample

And X

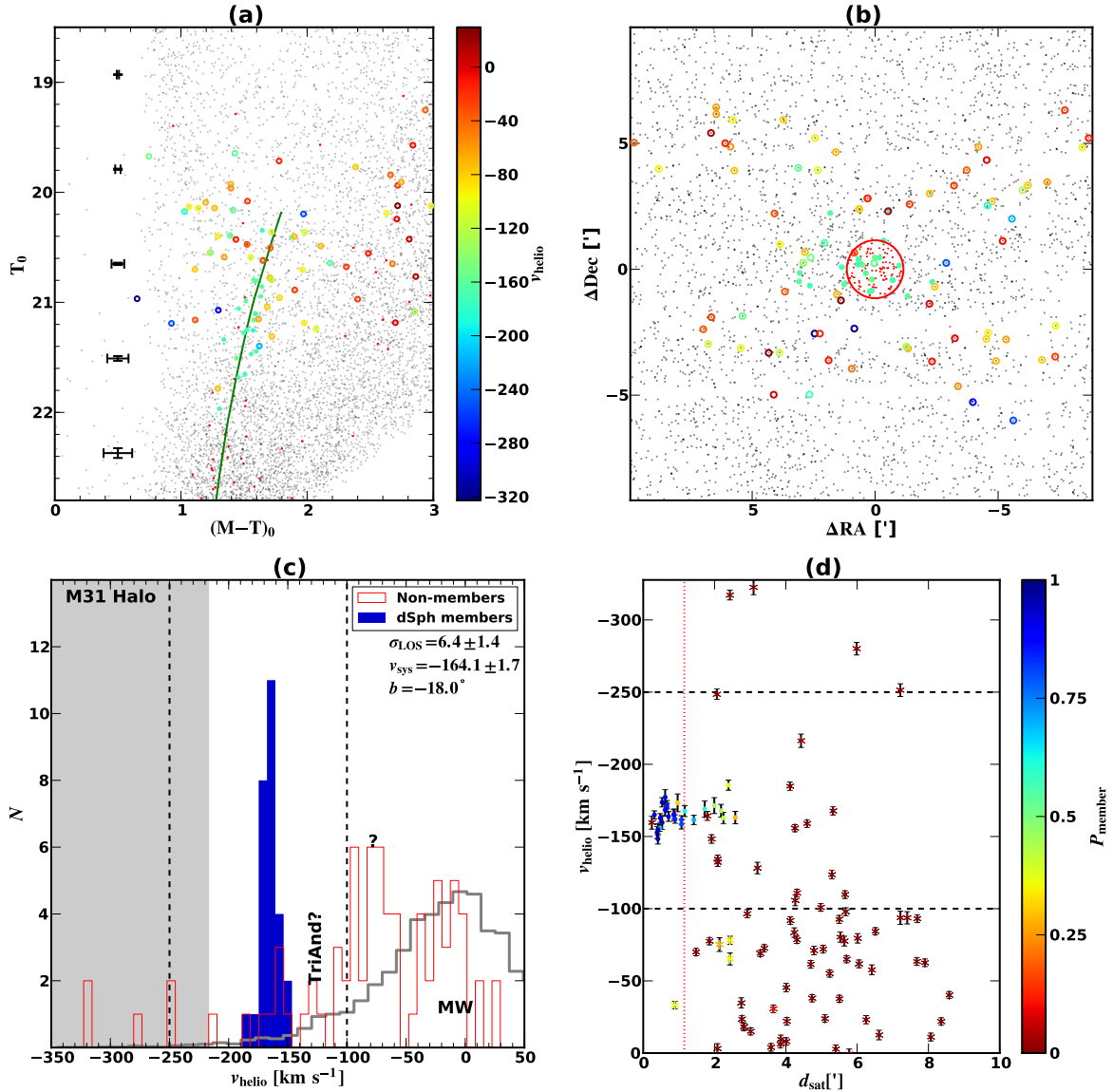


FIG. 13.— Same as Figure 5, but for And X.

and a more sophisticated treatment of errors. In addition, the M - R relation shows a detectable slope for the M31 dSphs, and thus we perform an error-weighted fit to a power law (dashed blue line in Figure 24), finding $\log(M_{1/2}) = 2.1 \log(r_{1/2}) + 8.1$. We conclude that at least our subset of the MW and M31 dSph populations are consistent with lying in the same distribution in major scaling relations.

Despite overall consistency between the scaling relations of the MW and M31 satellites, there are interesting outliers from the overall trends. In the M - R plane, there are two satellites that show significant deviation from the relation that both MW and M31 satellites seem to follow: And XIV and And XXII. The error bars for And XXII are large due to the poorly-constrained velocity dispersion, so its interpretation is unclear. However, And XIV is quite secure and shows a slightly larger $r_{1/2}$ for its mass than the other satellites (or a small mass for its

$r_{1/2}$). And XIV is already unusual in having a large v_{sys} , which has motivated the suggestion that it is only now falling into the M31 system for the first time (Majewski et al. 2007). The fact that it lies relatively distinct from the other satellites in the scaling relations serves to lend further weight to this idea, and supports the notion that environment leaves an observable mark on the structural properties of satellites even in low-density groups like the LG (e.g., Mayer et al. 2001; Kazantzidis et al. 2011b; Tollerud et al. 2011a).

In addition, And XV and XVI stand out as outliers from the other satellites in the M - L plane, in the sense that they are under-massive (both for luminosity and size). For And XVI, the error bars are very large, admitting a reasonable chance that the satellite lies on the relation with the other satellites, but And XV is more secure. An offset for And XV is perhaps not surprising however, as it shows hints of tidal interaction, as noted

And XI

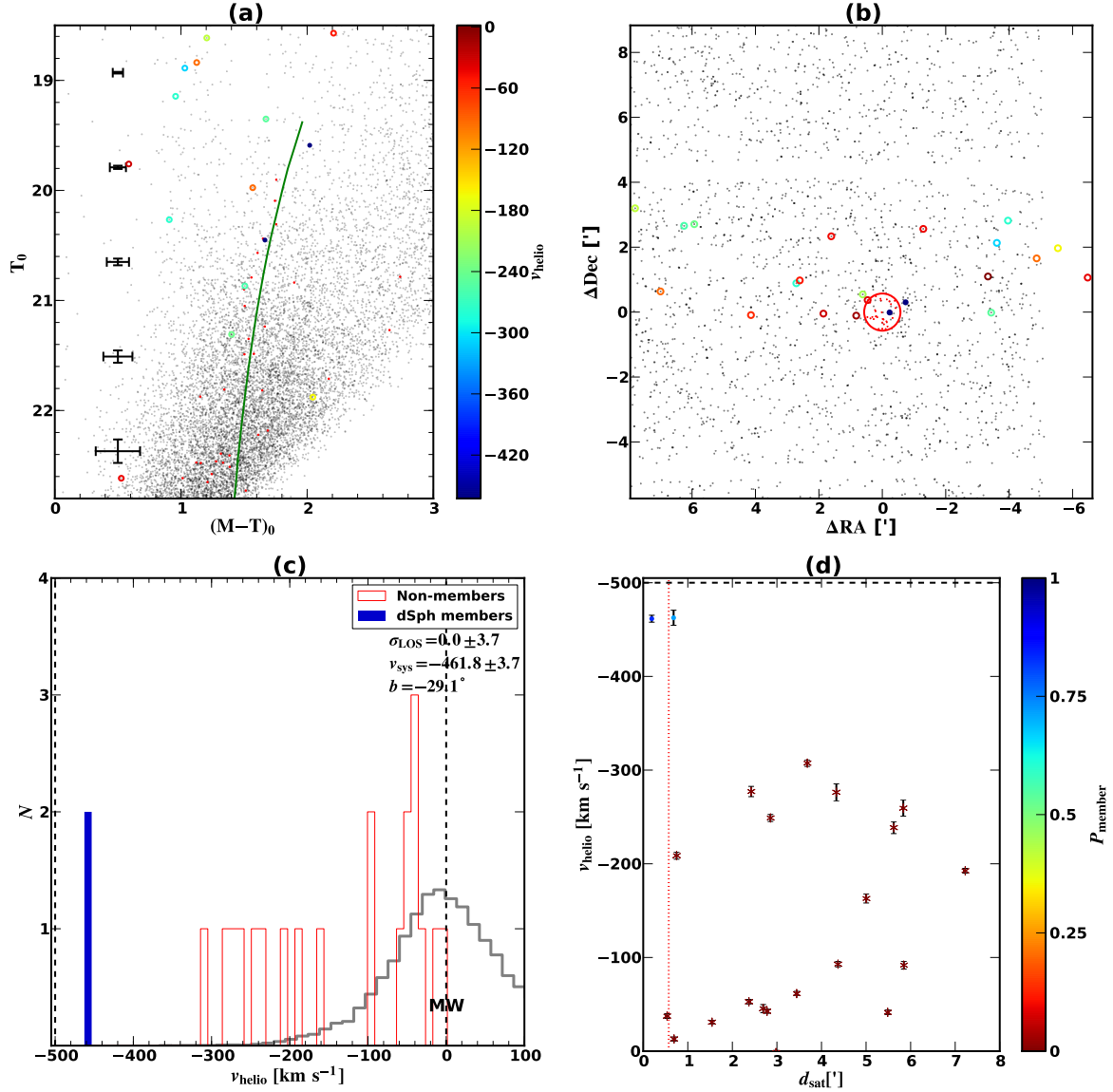


FIG. 14.— Same as Figure 5, but for And XI.

in §4.11. This is not entirely satisfying, however, as the presence of tidally stripped or halo contaminant stars would typically serve to *increase* the velocity dispersion. While its outlier status may be explained by statistical fluctuation, further investigation of this dSph is needed to resolve this oddity.

An additional exercise is suggested in the lower-right panel of Figure 24. The lowest dashed (black) line indicates the line corresponding to a mass-to-light ratio (with $r_{1/2}$) of 1. It is clear that the satellites lie far above this, indicating that they are dark matter-dominated galaxies with mass-to-light ratios higher than that expected from any reasonable stellar population. This warrants considering what dark matter halos they would be expected to inhabit to give the central densities observed here under the assumption that Λ CDM holds.

We map galaxies onto their dark matter halos by generating a series of NFW halo profiles (Navarro et al. 1997)

and determining the choice of halo that best fits each satellite in the M - R plane. This approach is described in detail by Tollerud et al. (2011b), and we only summarize here, highlighting the differences. In summary, we take the $M_{1/2}$ and $r_{1/2}$ estimators from the MRL space to deduce the central density of the dSphs studied here. Because Λ CDM dark matter halos are a one-parameter family, we can then map these galaxy scalings onto their dark matter halos by simply matching central densities, and reading off the implied dark matter halo’s virial mass.

Because we are examining satellites instead of isolated halos, the appropriate dark matter halos to compare to are *subhalos* of $M_{\text{vir}} \sim 10^{12} M_\odot$ hosts. For subhalos the concept of M_{vir} is not always well-defined, as their formal virial radii can reach to radii where the host halo is dominant. Additionally, tidal stripping alters the shape and total mass of a subhalo, particularly in its outer reaches.

And XII

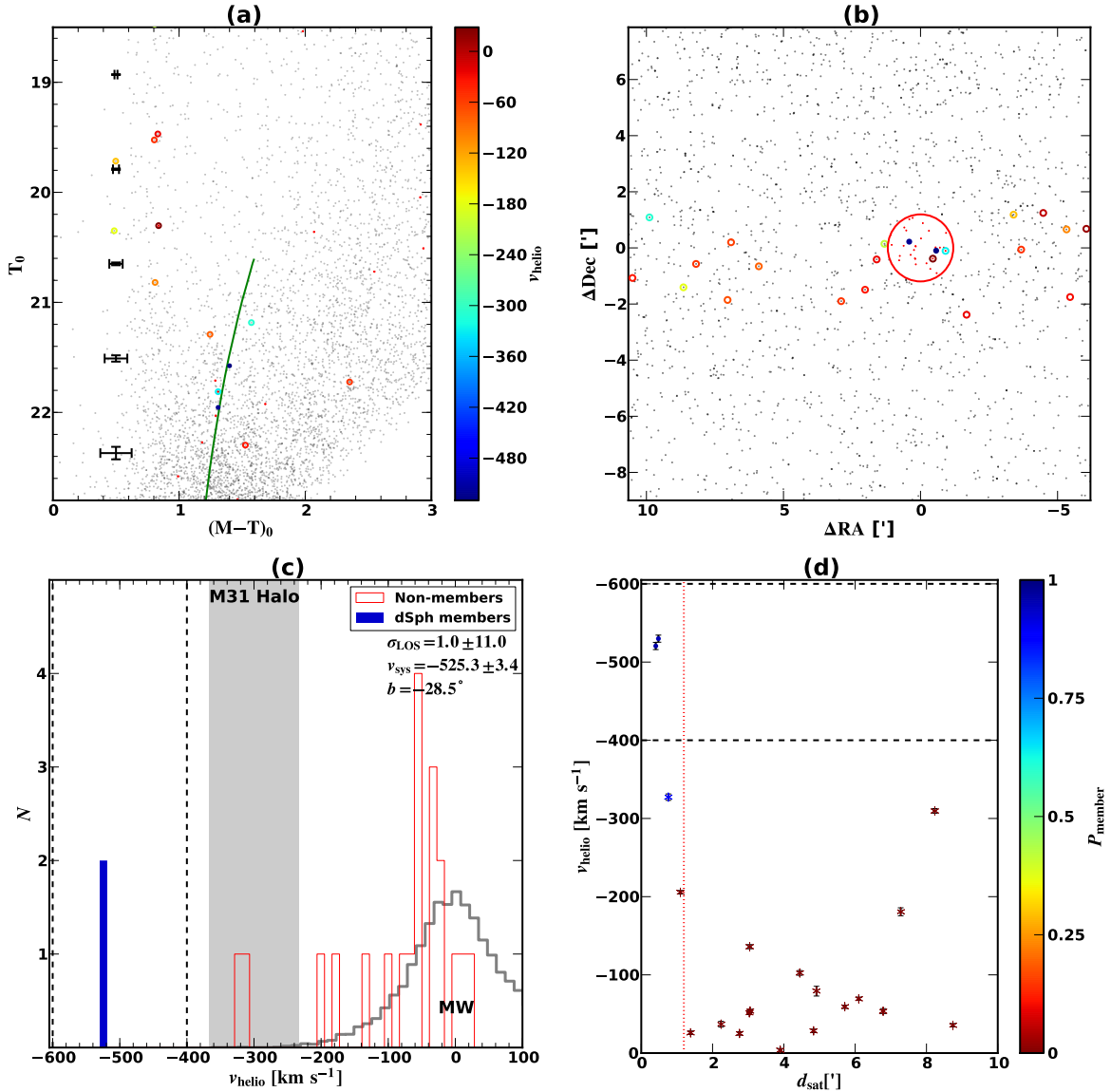


FIG. 15.— Same as Figure 5, but for And XII.

While this stripping does not have as strong of an impact on the central regions where the luminous galaxy sits until the satellite is nearly disrupted (Muñoz et al. 2008; Peñarrubia et al. 2009), it does alter the mass of the dark matter subhalo relative to isolated/field halos. Thus, we use V_{max} , the maximum circular velocity of a subhalo (where $V_{\text{circ}}(r) = GM(< r)/r$), as a more stable and well-defined parameter for the mass of a subhalo (e.g., Conroy et al. 2006; Moster et al. 2010; Boylan-Kolchin et al. 2010). Additionally, to reduce NFW to a one-parameter family of models, we use the $r_{V_{\text{max}}}$ - V_{max} relation from the Aquarius project for *subhalos*, rather than a field concentration-mass relation (Springel et al. 2008; Neto et al. 2007).

With this method used to map from the R - M scalings to dark matter halos, we plot the V_{max} values for the M31 and MW dSphs in Figure 25. While there is significantly more scatter here than in the MRL relations, this

is primarily because the error bars are relatively large, as the V_{max} of a subhalo is quite sensitive to the central density around the scales of these dSphs. Again, there is no definitive sign that these distributions for the MW and M31 are disjoint. Furthermore, taken together with error bars, there is no clear sign that dark matter halo mass scales appreciably with luminosity at these scales. *This suggests that the same common mass/halo profile for MW dSphs (Strigari et al. 2008; Walker et al. 2009) holds for M31 dSphs as well.*

As in the MRL relations, And XIV, And XV, And XVI and And XXII are outliers in Figure 25. This reveals a possible interpretation of these results: that these dSphs have anomalously small dark matter halos. In the case of And XV this is not necessarily surprising, as the hints of tidal features suggest it may be heavily stripped. And XXII and And XVI have large error bars that admit masses well above 10 km s^{-1} . For And XIV (and

And XIII

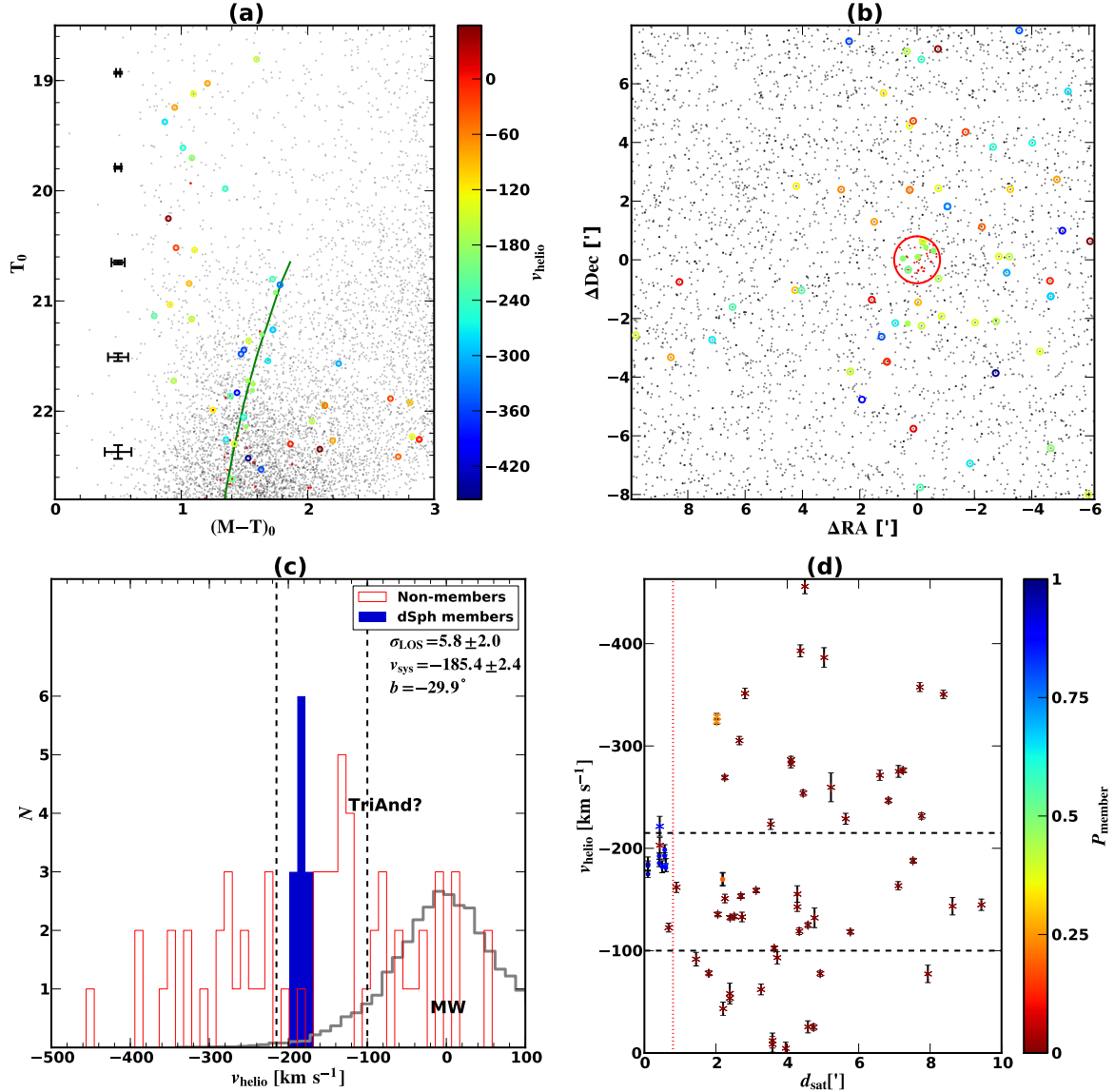


FIG. 16.— Same as Figure 5, but for And XIII.

the MW dSph Boötes I), the low mass is a puzzle, because it is below $10\text{--}15 \text{ km s}^{-1}$, the scale below which atomic hydrogen cooling becomes inefficient. Hence, if And XVI (and possibly XXII, XVI, or Boötes I) has not been disturbed by interactions, the density implies a dark matter halo that should never have formed galaxies following standard prescriptions of galaxy formation (e.g., Benson et al. 2002; Stringer et al. 2010; Kravtsov 2010). Clearly further investigation is warranted.

6. M31 MASS ESTIMATE

In addition to the properties of the dSphs on their own, the kinematics of M31 satellites as a system can be used to estimate the mass of M31 itself (e.g., Evans et al. 2000). While detailed modeling of such systems can provide in-depth dynamical information (Evans et al. 2000; Klypin et al. 2002; Watkins et al. 2010, e.g.), here we adopt a simple method, given the relatively small number of

TABLE 4
DERIVED QUANTITIES FOR M31 dSPH.

dSph Name	$\log(M_{1/2}/M_\odot)$	$\log(r_{1/2}/\text{kpc})$	$\log(L_{1/2}/L_\odot)$
And I	7.78 ± 0.18	-0.08 ± 0.02	6.65 ± 0.40
And III	7.50 ± 0.13	-0.28 ± 0.00	6.01 ± 0.12
And V	7.53 ± 0.12	-0.35 ± 0.02	5.77 ± 0.12
And VII	8.06 ± 0.09	-0.01 ± 0.02	7.25 ± 0.12
And IX	7.78 ± 0.20	-0.14 ± 0.02	5.17 ± 0.16
And X	6.94 ± 0.22	-0.51 ± 0.04	4.88 ± 0.03
And XIII	6.79 ± 0.38	-0.57 ± 0.06	4.61 ± 0.16
And XIV	7.03 ± 0.19	-0.27 ± 0.03	5.32 ± 0.03
And XV	6.60 ± 0.36	-0.45 ± 0.05	5.85 ± 0.16
And XVI	6.26 ± 0.74	-0.75 ± 0.04	5.61 ± 0.20
And XVIII	7.43 ± 0.24	-0.38 ± 0.03	5.80 ± 0.03
And XXI	7.56 ± 0.72	0.01 ± 0.03	5.66 ± 0.03
And XXII	6.67 ± 1.08	-0.27 ± 0.03	4.41 ± 0.06

tracer particles available here (i.e., the plausible satellites).

And XIV

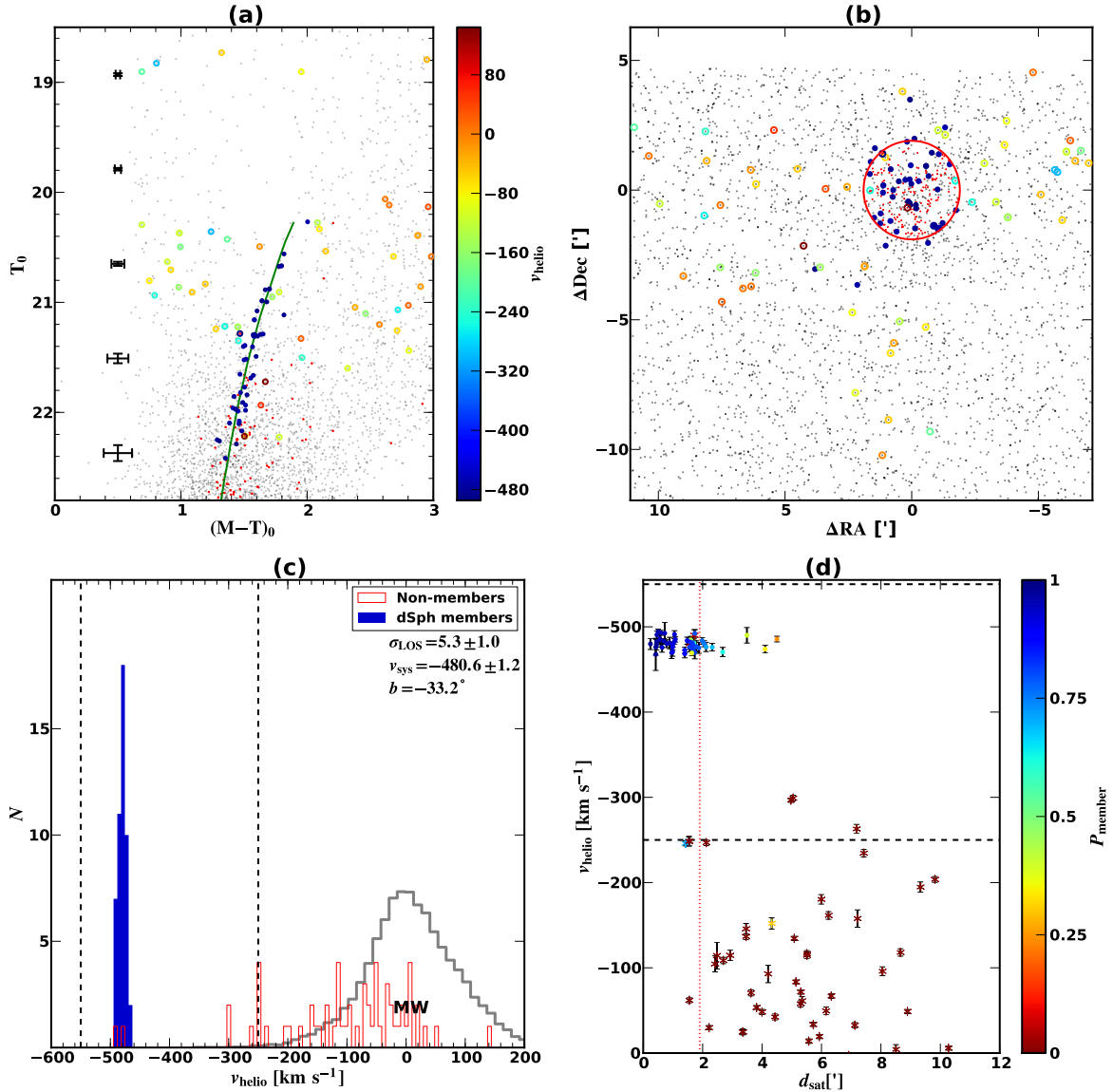


FIG. 17.— Same as Figure 5, but for And XIV.

We begin by estimating the distribution of v_{sys} for the M31 satellites. We use the v_{sys} values from Table 3, but with three changes. First, we do not make use of And XVIII given the fact that its distance may imply it is not a member of the M31 system (see discussion in §4.13). Second, we add And II, for which we adopt the $v_{\text{sys}} = -193.6 \pm 1.0$ and $d_{\text{M31}} = 185$ kpc from the distance measurement of McConnachie & Irwin (2006). Third, we also add in M31’s dE population: NGC 205, NGC 185, NGC 147, and M32. We obtain v_{sys} and distances for the first three from Geha et al. (2006) and Geha et al. (2010), while for M32 we adopt values from Evans et al. (2000). With those changes, we use the maximum likelihood technique described in §3.3 (Equation 2) to estimate the parameters of a Gaussian distribution of the dSph’s v_{sys} . The resulting mean $v_{\text{dsphs}} = -298 \pm 26$ km s⁻¹ of the M31 dSph system *as a whole* is consistent with the mean velocity of M31 and its stellar halo

(Guhathakurta et al. 2005, 2006; Chapman et al. 2006; Gilbert et al. 2007).

To infer a mass estimate from this distribution, we adopt an empirical approach appropriate for a Λ CDM context. We adopt a mass estimator proportional to the square of the velocity dispersion, which by dimensional analysis should have the form

$$M_{\text{est}}(< r) = c(r)\sigma^2 r/G, \quad (3)$$

where σ is the velocity dispersion, r is a radius, G is the gravitational constant, and c is a factor to be empirically determined¹⁵. To determine this factor, we make use of subhalos with $V_{\text{max}} > 5$ km s⁻¹ in the Via Lactea 2 simulation (VL2, Diemand et al. 2008). Kinematics of subhalos of the VL2 halo “observed” from a vantage point as

¹⁵ this estimator is inaccurately described in some contexts as a “virial estimator”; see e.g., Merritt (1987) Appendix A

And XV

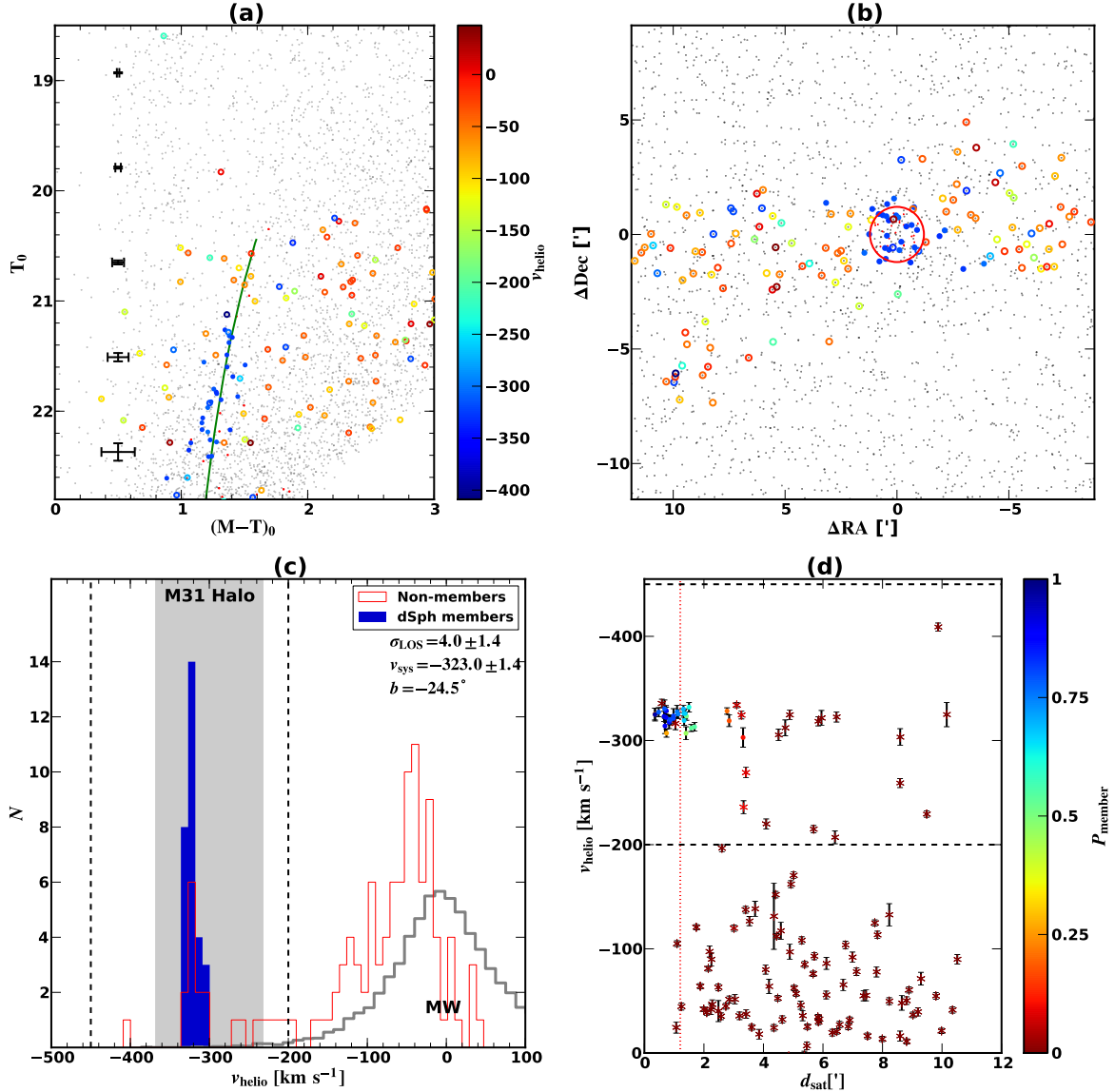


FIG. 18.— Same as Figure 5, but for And XV.

far from the center of the simulated halo as M31 is from the Sun provide a plausible sample of proxies for the M31 satellites. For the radius r within which we measure the mass, we adopt the median (3D) distance from M31 of the satellite sample, 139 kpc. The median is used here to reduce the effect of small number statistics, but our final virial mass estimate is not very sensitive to the choice of distance, as the correction factor adjusts for different measurement distances. We then determine the correction factor as $c(r) = M_{\text{true}}(< 139 \text{ kpc})/M_{\text{est}}(c = 1)$ for 1000 random orientations of the VL2 halo. The median and 68% tails of the c distribution are $c(r) = 1.96^{+0.37}_{-0.27}$. We note that this coefficient is somewhat different from the analytically-derived Wolf et al. (2010) mass estimator of the same form. This difference is a result of the fact that the Wolf et al. (2010) estimator requires that the full set of tracers be available for computing the half-light radius and velocity dispersion, which is not the case here

because the satellite population's completeness is only well-defined to the limits of the PAndAS survey.

With this correction factor in hand, we use Equation 3 with this value of c and propagate errors for c and σ to provide a mass estimate for M31 within 139 kpc of $M_{\text{M31}}(< 139 \text{ kpc}) = 8.0^{+4.1}_{-3.7} \times 10^{11} M_{\odot}$. With a mass within a fixed radius, we are in a position to estimate the virial mass of M31's dark matter halo. We follow the approach of Tollerud et al. (2011b), and use a grid of NFW halos following the *field* $c - M_{\text{vir}}$ relation of Klypin et al. (2010), choosing one based on the $M_{\text{M31}}(r < 139 \text{ kpc})$ determined above. This results in a virial mass for M31 of $M_{\text{vir}} = 1.2^{+0.9}_{-0.7} \times 10^{12} M_{\odot}$. This corrected result is comparable to the results of Evans et al. (2000) and Watkins et al. (2010), and thus suggests a moderately lower mass than expected based on assuming abundance matching, i.e., a monotonic halo mass to galaxy luminosity mapping ($\sim 3 \times 10^{12} M_{\odot}$ based on Guo et al. 2010).

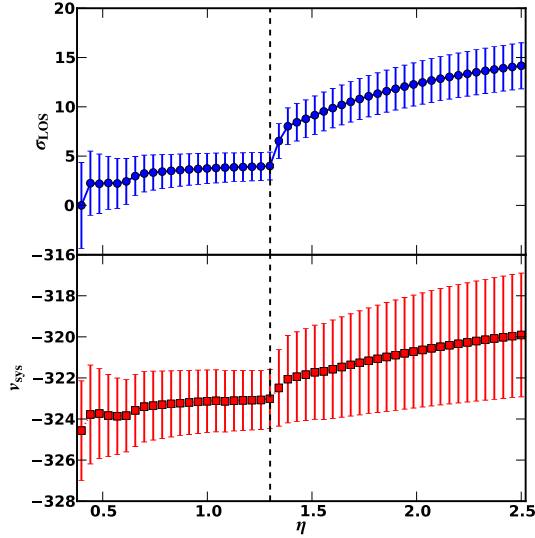


FIG. 19.— Similar as Figure 6, but for And XV. The x-axis has been more densely sampled relative to Figure 6 to better capture the variation near the chosen η value.

7. CONCLUSIONS

In this paper, we have described spectroscopy of M31 dSph satellites as part of the SPLASH Survey. We filter out MW foreground and M31 halo field contamination to identify M31 dSph member stars, and use these data to determine v_{sys} and σ_{LOS} for the satellites. Based on these kinematics, we determine for each dSph the implied mass within the half light radius, and (under the assumption that these objects are dark matter-dominated) we estimate their dark halo properties. This paper can be summarized as follows:

1. We provide a homogenous spectroscopic survey of 15 M31 dSphs and provide radial velocities of resolved stars in these galaxies.
2. We confirm that And XVIII, XXI, and XXII are kinematically cold and hence likely true satellite galaxies.
3. We find that And XXII has a v_{sys} close to with M33, suggesting it is associated with M33 rather than M31. If so, this is likely the first large mass ratio sub-subhalo (or satellite of a satellite) known.
4. We find that the M31 dSphs obey very similar mass-size-luminosity scalings to those of MW satellites. This suggests that the MW satellite population is not particularly unique and may be typical of a starforming L_* galaxy.
5. We use the scalings of the M31 dSphs to infer properties of their dark matter halos. The masses of these halos show no sign of scaling with luminosity, similar to the MW dSphs (Strigari et al. 2008; Walker et al. 2009).
6. And XIV, as well as perhaps And XV and And XVI, show densities consistent with dark matter halos with $V_{\text{max}} < 10 \text{ km s}^{-1}$ (although consistent with higher masses at $\sim 1\sigma$). If the most-likely masses for these systems are correct, these (along

with the MW satellite Boötes I) are the lowest-mass dark matter halos hosting stars, with potential well depths indicative of field halos that are below the atomic hydrogen cooling limit.

7. Using the systemic velocities of M31 dSphs as tracer particles and adopting an empirical mass estimator suggested by n-body simulations, we estimate the mass of M31 within 139 kpc to be $M_{\text{M31}}(< 139 \text{ kpc}) = 8.0^{+4.1}_{-3.7} \times 10^{11} M_{\odot}$. This corresponds to a virial mass for M31's dark matter halo of $M_{\text{vir}} = 1.2^{+0.9}_{-0.7} \times 10^{12} M_{\odot}$.

This analysis of M31 dSphs thus represent a major step forward in understanding the faintest known class of galaxies. The M31 satellites present an opportunity to understand these galaxies in a new way, as a system, along with their host halo, providing a rich set of opportunities for examining galaxy formation and Λ CDM. Their similarity to MW dSphs also confirm of the Copernican principle, affirming that the MW may be a typical galaxy with typical satellites, albeit in an extraordinary universe.

We wish to acknowledge Nhung Ho, Greg Martinez, and Ricardo Munoz for helpful discussions.

EJT acknowledges support from a Graduate Assistance in Areas of National Need (GAANN) fellowship. RLB acknowledges receipt of the the Mark C. Pirrung Family Graduate Fellowship from the Jefferson Scholars Foundation and a Fellowship Enhancement for Outstanding Doctoral Candidates from the Office of the Vice President of Research at the University of Virginia. MG acknowledges support from NSF grant AST-0908752 and the Alfred P. Sloan Foundation. PG, JSB, and SRM acknowledge support from collaborative NSF grants AST-1010039, AST-1009973, AST-1009882, and AST-0607726. AC thanks the UC Santa Cruz Science Internship Program for support. Additional support for this work was provided by NASA through Hubble Fellowship grants 51256.01 and 51273.01 awarded to ENK and KMG by the Space Telescope Science Institute, which is operated by the Association of Universities for Research in Astronomy, Inc., for NASA, under contract NAS 5-26555.

The spec2d pipeline used to reduce the DEIMOS data was developed at UC Berkeley with support from NSF grant AST-0071048.

The authors wish to recognize and acknowledge the very significant cultural role and reverence that the summit of Mauna Kea has always had within the indigenous Hawaiian community. We are most fortunate to have the opportunity to conduct observations from this mountain.

Some slitmasks were designed based on data acquired using the Large Binocular Telescope (LBT). The LBT is an international collaboration among institutions in the United States, Italy and Germany. LBT Corporation partners are: The University of Arizona on behalf of the Arizona university system; Istituto Nazionale di Astrofisica, Italy; LBT Beteiligungsgesellschaft, Germany, representing the Max-Planck Society, the Astrophysical Institute Potsdam, and Heidelberg University; The Ohio State University, and The Research Corporation, on be-

And XVI

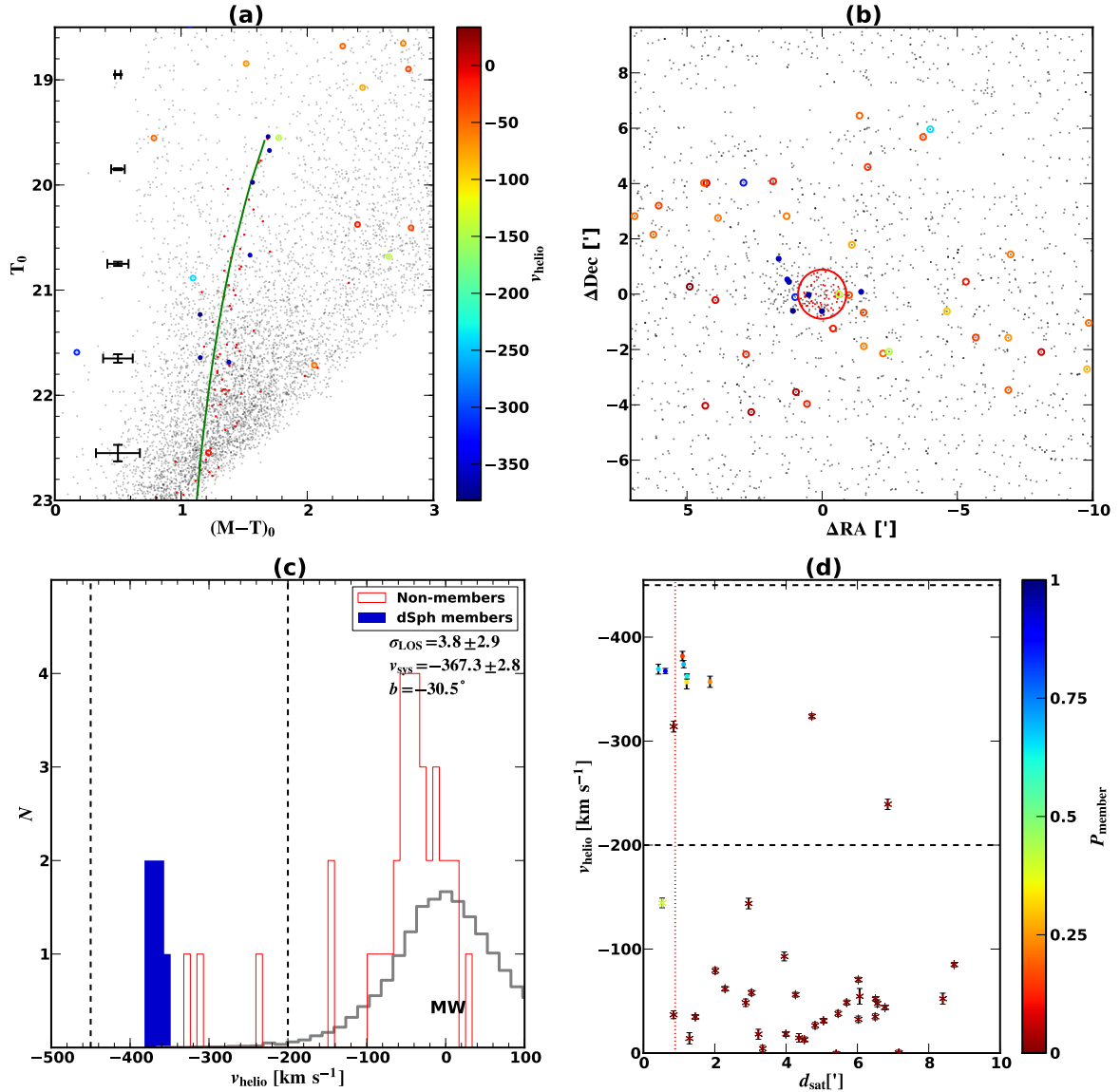


FIG. 20.— Same as Figure 5, but for And XVI.

half of The University of Notre Dame, University of Minnesota and University of Virginia.

This research used the facilities of the Canadian Astronomy Data Centre operated by the National Research

Council of Canada with the support of the Canadian Space Agency.

REFERENCES

- Adelman-McCarthy, J. K. et al. 2006, *ApJS*, 162, 38, arXiv:astro-ph/0507711
- Armandroff, T. E., Davies, J. E., & Jacoby, G. H. 1998, *AJ*, 116, 2287, arXiv:astro-ph/9807232
- Bell, E. F., Slater, C. T., & Martin, N. F. 2011, *ApJ*, 742, L15, 1110.5906
- Benson, A. J., Lacey, C. G., Baugh, C. M., Cole, S., & Frenk, C. S. 2002, *MNRAS*, 333, 156, arXiv:astro-ph/0108217
- Binney, J., & Tremaine, S. 2008, *Galactic Dynamics: Second Edition* (Princeton University Press)
- Bovill, M. S., & Ricotti, M. 2009, *ApJ*, 693, 1859, 0806.2340
- Boylan-Kolchin, M., Bullock, J. S., & Kaplinghat, M. 2011, ArXiv e-prints, 1103.0007
- Boylan-Kolchin, M., Springel, V., White, S. D. M., & Jenkins, A. 2010, *MNRAS*, 406, 896, 0911.4484
- Bradford, J. D. et al. 2011, ArXiv e-prints, 1110.0484
- Brasseur, C. M., Martin, N. F., Macciò, A. V., Rix, H.-W., & Kang, X. 2011, ArXiv e-prints, 1106.5500
- Bullock, J. S. 2010, ArXiv e-prints, 1009.4505
- Bullock, J. S., & Johnston, K. V. 2005, *ApJ*, 635, 931, arXiv:astro-ph/0506467
- Bullock, J. S., Kravtsov, A. V., & Weinberg, D. H. 2000, *ApJ*, 539, 517, arXiv:astro-ph/0002214
- Chapman, S. C. et al. 2008, *MNRAS*, 390, 1437, 0808.0755
- Chapman, S. C., Ibata, R., Lewis, G. F., Ferguson, A. M. N., Irwin, M., McConnachie, A., & Tanvir, N. 2005, *ApJ*, 632, L87, arXiv:astro-ph/0506103

And XVIII

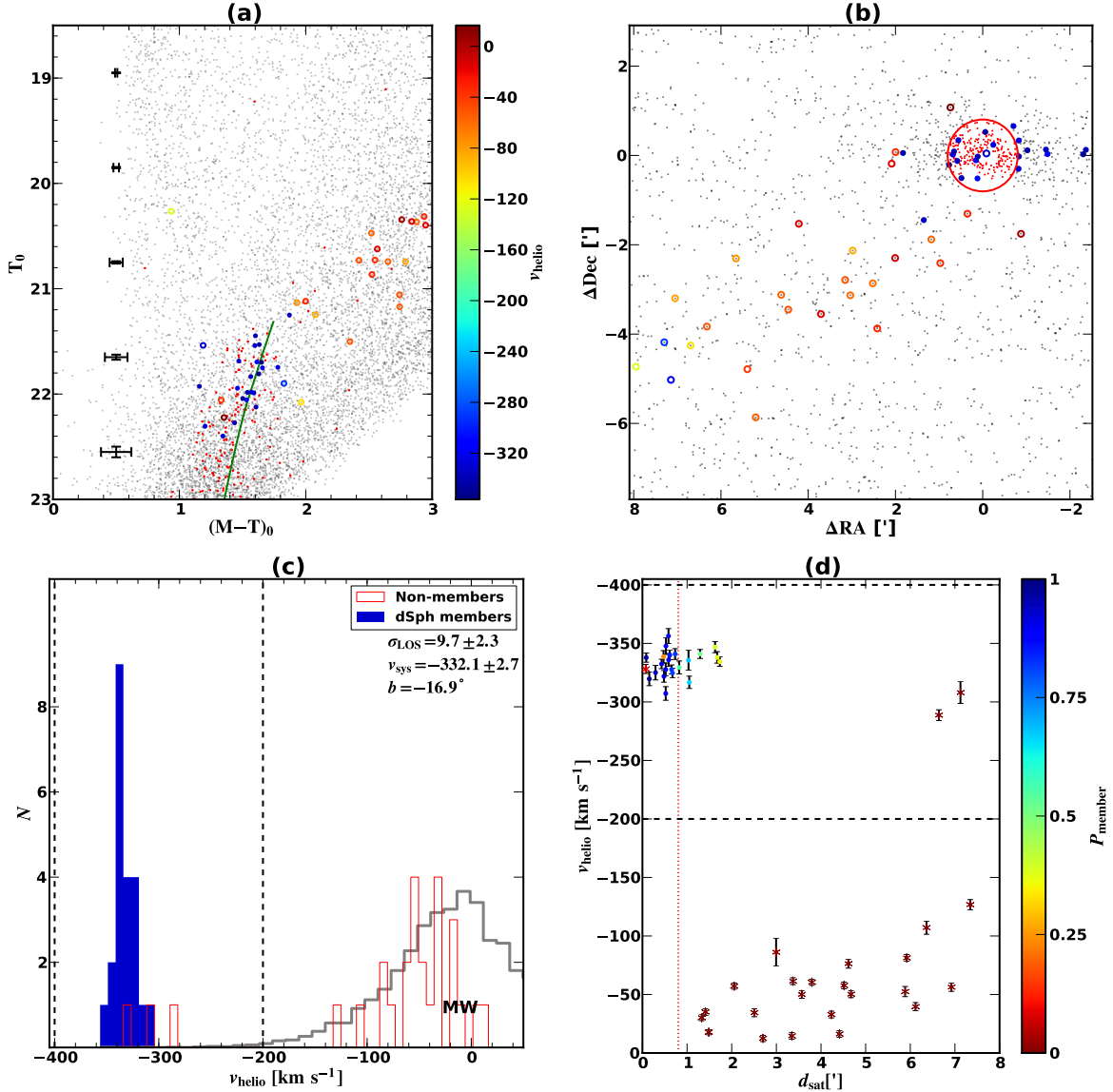


FIG. 21.— Same as Figure 5, but for And XVIII.

—, 2006, *ApJ*, 653, 255, arXiv:astro-ph/0602604
 Chapman, S. C. et al. 2007, *ApJ*, 662, L79, 0705.4113
 Collins, M. L. M. et al. 2010, *MNRAS*, 407, 2411, 0911.1365
 Conroy, C., Wechsler, R. H., & Kravtsov, A. V. 2006, *ApJ*, 647, 201, arXiv:astro-ph/0512234
 Côté, P., Mateo, M., Olszewski, E. W., & Cook, K. H. 1999, *ApJ*, 526, 147, arXiv:astro-ph/9907003
 Crane, J. D., Majewski, S. R., Rocha-Pinto, H. J., Frinchaboy, P. M., Skrutskie, M. F., & Law, D. R. 2003, *ApJ*, 594, L119, arXiv:astro-ph/0307505
 Diemand, J., Kuhlen, M., Madau, P., Zemp, M., Moore, B., Potter, D., & Stadel, J. 2008, *Nature*, 454, 735, 0805.1244
 Durrell, P. R. et al. 2007, *ApJ*, 656, 746, arXiv:astro-ph/0611180
 Evans, N. W., Wilkinson, M. I., Guhathakurta, P., Grebel, E. K., & Vogt, S. S. 2000, *ApJ*, 540, L9, arXiv:astro-ph/0008155
 Ferguson, A. M. N., Gallagher, J. S., & Wyse, R. F. G. 2000, *AJ*, 120, 821, arXiv:astro-ph/0005015
 Font, A. S. et al. 2011, *ArXiv e-prints*, 1103.0024
 Geha, M., Guhathakurta, P., Rich, R. M., & Cooper, M. C. 2006, *AJ*, 131, 332, arXiv:astro-ph/0509561
 Geha, M., van der Marel, R. P., Guhathakurta, P., Gilbert, K. M., Kalirai, J., & Kirby, E. N. 2010, *ApJ*, 711, 361, 0911.3654

Gilbert, K. M. et al. 2007, *ApJ*, 668, 245, arXiv:astro-ph/0703029
 —, 2006, *ApJ*, 652, 1188, arXiv:astro-ph/0605171
 —, 2009, *ApJ*, 705, 1275, 0909.4540
 Girardi, L., Bertelli, G., Bressan, A., Chiosi, C., Groenewegen, M. A. T., Marigo, P., Salasnich, B., & Weiss, A. 2002, *A&A*, 391, 195, arXiv:astro-ph/0205080
 Grcevich, J., & Putman, M. E. 2009, *ApJ*, 696, 385, 0901.4975
 Guhathakurta, P., Ostheimer, J. C., Gilbert, K. M., Rich, R. M., Majewski, S. R., Kalirai, J. S., Reitzel, D. B., & Patterson, R. J. 2005, *ArXiv Astrophysics e-prints*, arXiv:astro-ph/0502366
 Guhathakurta, P., Reitzel, D. B., & Grebel, E. K. 2000, in *Society of Photo-Optical Instrumentation Engineers (SPIE) Conference Series*, Vol. 4005, Society of Photo-Optical Instrumentation Engineers (SPIE) Conference Series, ed. J. Bergeron, 168–179, arXiv:astro-ph/0004371
 Guhathakurta, P. et al. 2006, *AJ*, 131, 2497, arXiv:astro-ph/0406145
 Guo, Q., White, S., Li, C., & Boylan-Kolchin, M. 2010, *MNRAS*, 404, 1111, 0909.4305
 Hammer, F., Puech, M., Chemin, L., Flores, H., & Lehnert, M. D. 2007, *ApJ*, 662, 322, arXiv:astro-ph/0702585

And XXI

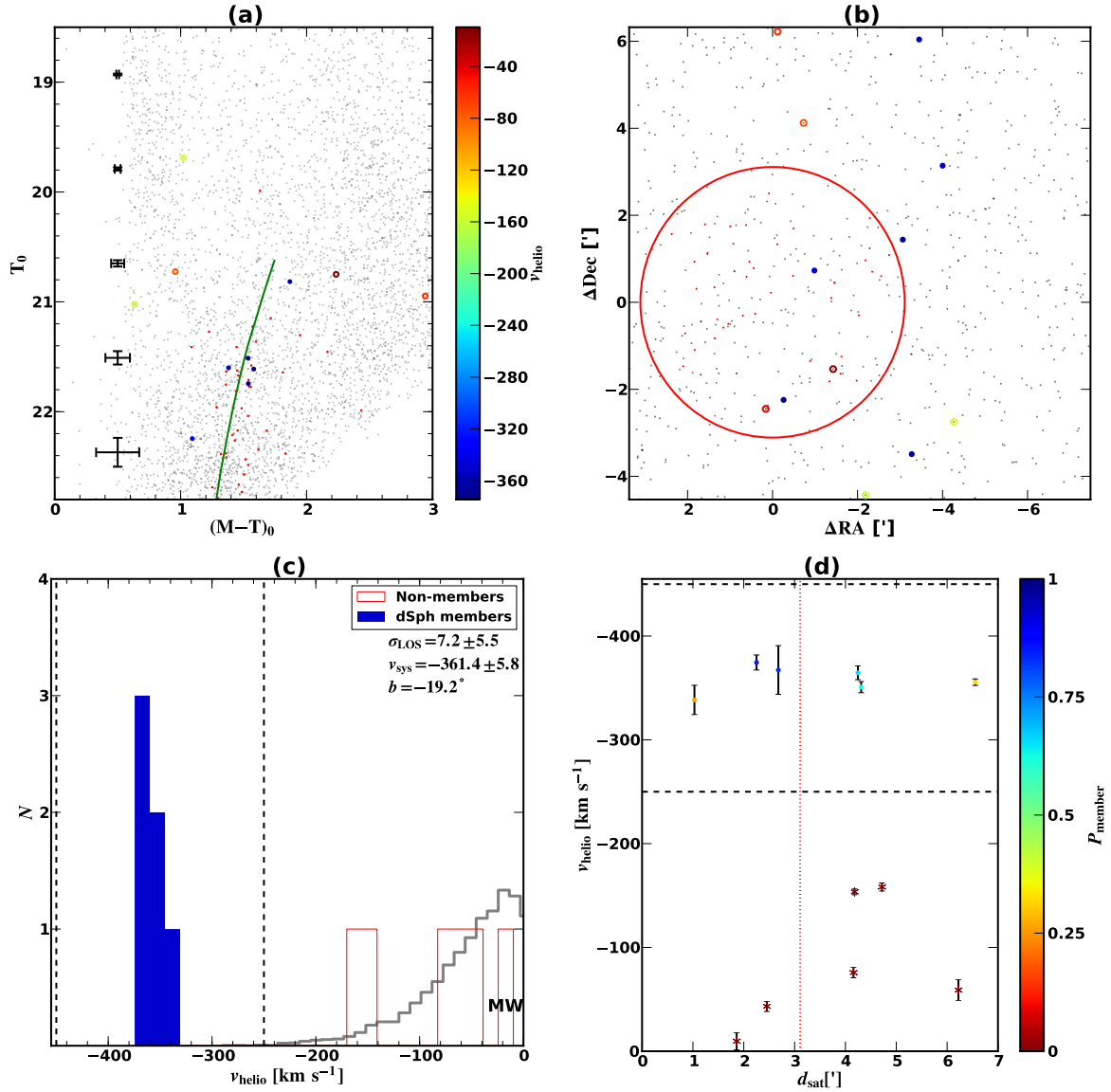


FIG. 22.— Same as Figure 5, but for And XXI.

Hilker, M., Mieske, S., & Infante, L. 2003, *A&A*, 397, L9, arXiv:astro-ph/0212044
 Horne, K. 1986, *PASP*, 98, 609
 Huchra, J. P., Vogeley, M. S., & Geller, M. J. 1999, *ApJS*, 121, 287
 Ibata, R., Chapman, S., Ferguson, A. M. N., Irwin, M., Lewis, G., & McConnachie, A. 2004, *MNRAS*, 351, 117, arXiv:astro-ph/0403068
 Ibata, R., Irwin, M., Lewis, G., Ferguson, A. M. N., & Tanvir, N. 2001, *Nature*, 412, 49, arXiv:astro-ph/0107090
 Ibata, R., Martin, N. F., Irwin, M., Chapman, S., Ferguson, A. M. N., Lewis, G. F., & McConnachie, A. W. 2007, *ApJ*, 671, 1591, 0704.1318
 Ibata, R. A., Irwin, M. J., Lewis, G. F., Ferguson, A. M. N., & Tanvir, N. 2003, *MNRAS*, 340, L21, arXiv:astro-ph/0301067
 Irwin, M. J., Ferguson, A. M. N., Huxor, A. P., Tanvir, N. R., Ibata, R. A., & Lewis, G. F. 2008, *ApJ*, 676, L17, 0802.0698
 Kalirai, J. S. et al. 2010, *ApJ*, 711, 671, 0911.1998
 ——. 2006, *ApJ*, 648, 389, arXiv:astro-ph/0605170
 ——. 2009, *ApJ*, 705, 1043, 0909.3298
 Karachentsev, I. D., & Karachentseva, V. E. 1999, *A&A*, 341, 355

Karachentsev, I. D., Karachentseva, V. E., & Huchtmeier, W. K. 2001, *A&A*, 366, 428
 Karachentseva, V. E., & Karachentsev, I. D. 1998, *A&AS*, 127, 409
 Kazantzidis, S., Lokas, E. L., Callegari, S., Mayer, L., & Moustakas, L. A. 2011a, *ApJ*, 726, 98, 1009.2499
 ——. 2011b, *ApJ*, 726, 98, 1009.2499
 Klypin, A., Kravtsov, A. V., Valenzuela, O., & Prada, F. 1999, *ApJ*, 522, 82, arXiv:astro-ph/9901240
 Klypin, A., Trujillo-Gomez, S., & Primack, J. 2010, *ArXiv e-prints*, 1002.3660
 Klypin, A., Zhao, H., & Somerville, R. S. 2002, *ApJ*, 573, 597, arXiv:astro-ph/0110390
 Koposov, S. E. et al. 2011, *ApJ*, 736, 146, 1105.4102
 Koposov, S. E., Yoo, J., Rix, H.-W., Weinberg, D. H., Macciò, A. V., & Escudé, J. M. 2009, *ApJ*, 696, 2179, 0901.2116
 Kravtsov, A. 2010, *Advances in Astronomy*, 2010, 0906.3295
 Letarte, B. et al. 2009, *MNRAS*, 400, 1472, 0901.0820
 Majewski, S. R. et al. 2007, *ApJ*, 670, L9, arXiv:astro-ph/0702635
 Majewski, S. R., Ostheimer, J. C., Kunkel, W. E., & Patterson, R. J. 2000, *AJ*, 120, 2550, arXiv:astro-ph/0006411
 Mancone, C., & Sarajedini, A. 2008, *AJ*, 136, 1913, 0808.3285

And XXII

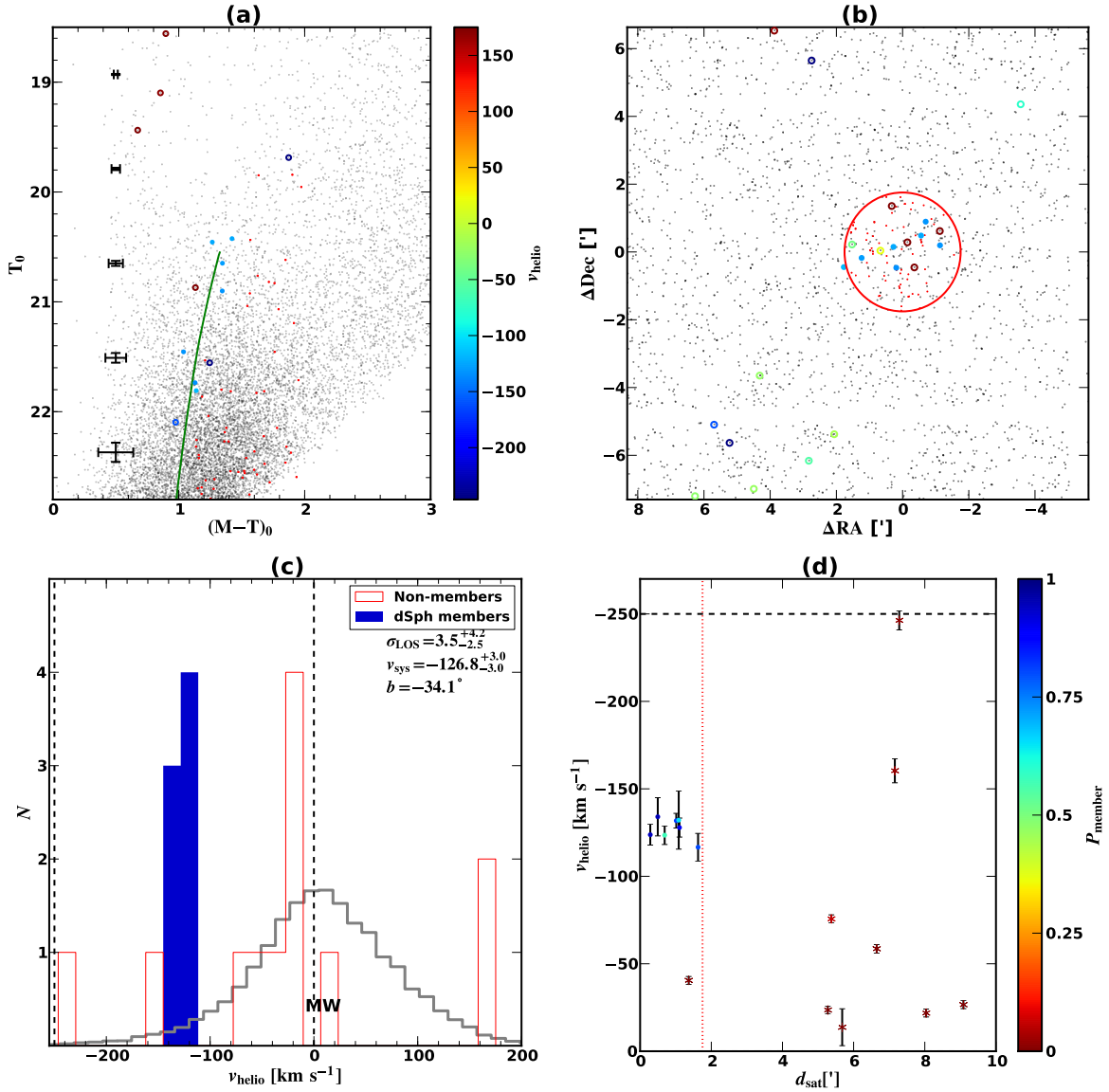


FIG. 23.— Same as Figure 5, but for And XXII.

Martin, N. F., Ibata, R. A., Irwin, M. J., Chapman, S., Lewis, G. F., Ferguson, A. M. N., Tanvir, N., & McConnachie, A. W. 2006, *MNRAS*, 371, 1983, arXiv:astro-ph/0607472
 Martin, N. F. et al. 2009, *ApJ*, 705, 758, 0909.0399
 Mateo, M. L. 1998, *ARA&A*, 36, 435, arXiv:astro-ph/9810070
 Mayer, L., Governato, F., Colpi, M., Moore, B., Quinn, T., Wadsley, J., Stadel, J., & Lake, G. 2001, *ApJ*, 559, 754, arXiv:astro-ph/0103430
 McConnachie, A., Irwin, M., Chapman, S., Ibata, R., Ferguson, A., Lewis, G., & Tanvir, N. 2005a, in *IAU Colloq. 198: Near-fields cosmology with dwarf elliptical galaxies*, ed. H. Jerjen & B. Binggeli, 84–91
 McConnachie, A. W. et al. 2008, *ApJ*, 688, 1009, 0806.3988
 McConnachie, A. W., & Irwin, M. J. 2006, *MNRAS*, 365, 1263, arXiv:astro-ph/0511004
 McConnachie, A. W., Irwin, M. J., Ferguson, A. M. N., Ibata, R. A., Lewis, G. F., & Tanvir, N. 2005b, *MNRAS*, 356, 979, arXiv:astro-ph/0410489
 McConnachie, A. W. et al. 2009, *Nature*, 461, 66, 0909.0398
 Merrett, H. R. et al. 2006, *MNRAS*, 369, 120, arXiv:astro-ph/0603125
 Merritt, D. 1987, *ApJ*, 313, 121

Minor, Q. E., Martinez, G., Bullock, J., Kaplinghat, M., & Trainor, R. 2010, *ApJ*, 721, 1142, 1001.1160
 Moore, B., Ghigna, S., Governato, F., Lake, G., Quinn, T., Stadel, J., & Tozzi, P. 1999, *ApJ*, 524, L19, arXiv:astro-ph/9907411
 Moster, B. P., Somerville, R. S., Maubetsch, C., van den Bosch, F. C., Macciò, A. V., Naab, T., & Oser, L. 2010, *ApJ*, 710, 903, 0903.4682
 Muñoz, R. R., Majewski, S. R., & Johnston, K. V. 2008, *ApJ*, 679, 346, 0712.4312
 Navarro, J. F., Frenk, C. S., & White, S. D. M. 1997, *ApJ*, 490, 493, arXiv:astro-ph/9611107
 Neto, A. F. et al. 2007, *MNRAS*, 381, 1450, 0706.2919
 Newberg, H. J. et al. 2002, *ApJ*, 569, 245, arXiv:astro-ph/0111095
 Nichols, M., & Bland-Hawthorn, J. 2011, *ApJ*, 732, 17, 1102.4849
 Ostriker, Jr., J. C. 2003, PhD thesis, UNIVERSITY OF VIRGINIA
 Paturel, G., Petit, C., Garnier, R., & Prugniel, P. 2000, *A&AS*, 144, 475
 Peñarrubia, J., Navarro, J. F., McConnachie, A. W., & Martin, N. F. 2009, *ApJ*, 698, 222, 0811.1579
 Richardson, J. C. et al. 2011, *ApJ*, 732, 76, 1102.2902

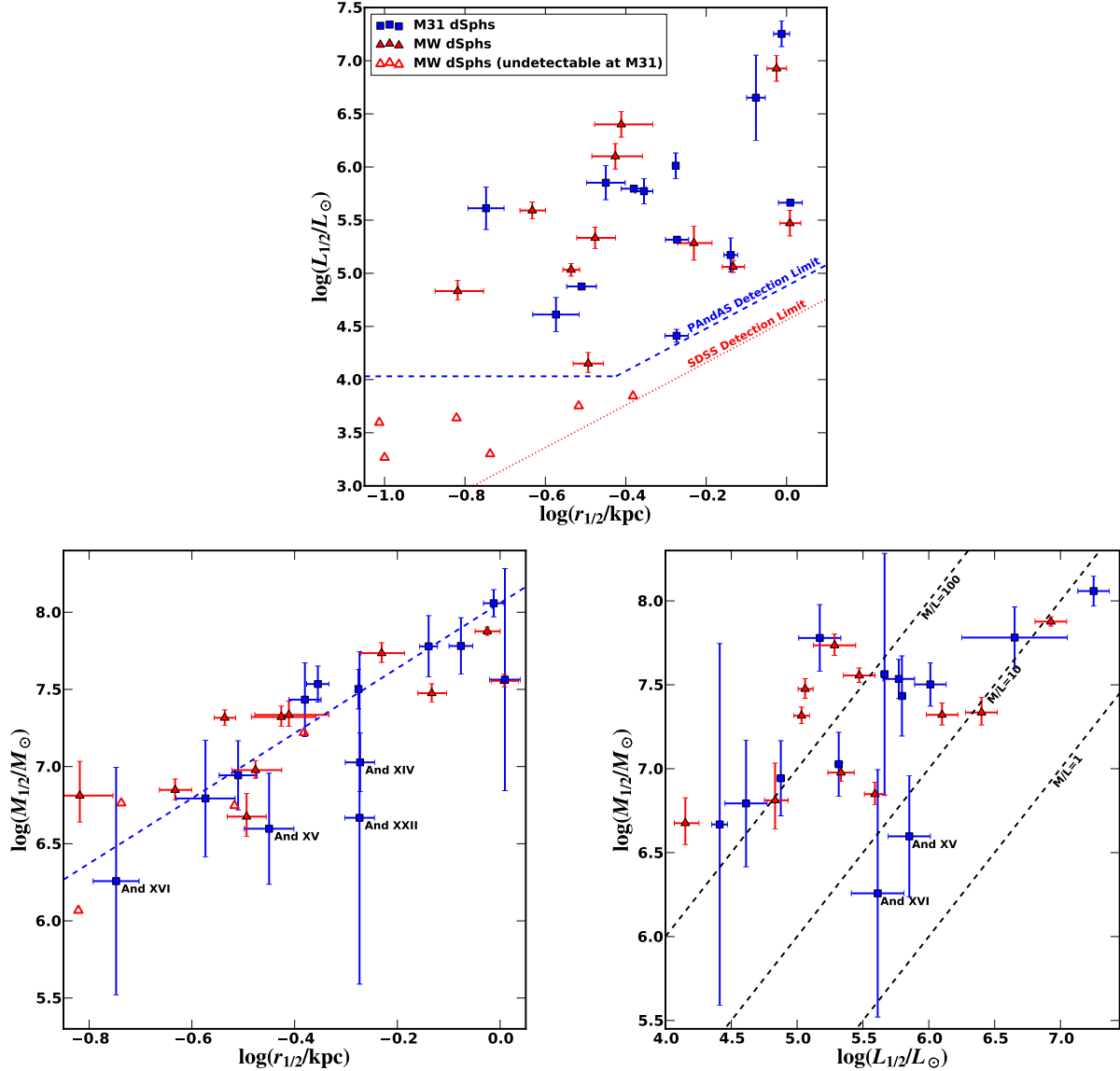


FIG. 24.— Representation of Local Group dSphs in the MRL space of Tollerud et al. (2011b). The upper panel shows the L-R plane (half-luminosity vs. deprojected half-light radius). Points (blue) are M31 dSphs, with associated error bars. Also shown are detection limits for SDSS searches of the MW (Tollerud et al. 2008) as the red dotted line, and M31 detection limits from the PAndAS survey as reported in Brasseur et al. (2011). Triangles (red) are MW dSphs as tabulated in Wolf et al. (2010), where solid triangles are within the M31 detection limit, and unfilled triangles are not. The same data set is shown in the R - M plane (mass within deprojected half-light radius vs. deprojected half-light radius) on lower left. The dashed (blue) line in this panel indicates the best-fit power law with slope 2.1. The lower-right panel shows the M - L plane (mass within deprojected half-light radius vs. half-luminosity), and the dashed (black) lines in the same panel indicate lines of mass-to-light ratios of 1, 10, and 100 M_{\odot}/L_{\odot} .

Robin, A. C., Reyl  , C., Derri  re, S., & Picaud, S. 2003, *A&A*, 409, 523
 Rocha-Pinto, H. J., Majewski, S. R., Skrutskie, M. F., Crane, J. D., & Patterson, R. J. 2004, *ApJ*, 615, 732, [arXiv:astro-ph/0405437](http://arxiv.org/abs/astro-ph/0405437)
 Schiavon, R. P., Barbuy, B., Rossi, S. C. F., & Milone, A. 1997, *ApJ*, 479, 902, [arXiv:astro-ph/9610243](http://arxiv.org/abs/astro-ph/9610243)
 Schlegel, D. J., Finkbeiner, D. P., & Davis, M. 1998, *ApJ*, 500, 525, [arXiv:astro-ph/9710327](http://arxiv.org/abs/astro-ph/9710327)
 Shapiro, S. S., & Wilk, M. B. 1965, *Biometrika*, 52, 591, <http://biomet.oxfordjournals.org/content/52/3-4/591.full.pdf+html>
 Simon, J. D., & Geha, M. 2007, *ApJ*, 670, 313, 0706.0516
 Simon, J. D. et al. 2011, *ApJ*, 733, 46, 1007.4198
 Slater, C. T., Bell, E. F., & Martin, N. F. 2011, *ApJ*, 742, L14, 1110.5903
 Sohn, S. T. et al. 2007, *ApJ*, 663, 960, [arXiv:astro-ph/0608151](http://arxiv.org/abs/astro-ph/0608151)
 Springel, V. et al. 2008, *MNRAS*, 391, 1685, 0809.0898

Strigari, L. E., Bullock, J. S., Kaplinghat, M., Diemand, J., Kuhlen, M., & Madau, P. 2007, *ApJ*, 669, 676, 0704.1817
 Strigari, L. E., Bullock, J. S., Kaplinghat, M., Simon, J. D., Geha, M., Willman, B., & Walker, M. G. 2008, *Nature*, 454, 1096, 0808.3772
 Stringer, M., Cole, S., & Frenk, C. S. 2010, *MNRAS*, 404, 1129, 0911.1888
 Tollerud, E. J., Boylan-Kolchin, M., Barton, E. J., Bullock, J. S., & Trinh, C. Q. 2011a, *ApJ*, 738, 102, 1103.1875
 Tollerud, E. J., Bullock, J. S., Graves, G. J., & Wolf, J. 2011b, *ApJ*, 726, 108, 1007.5311
 Tollerud, E. J., Bullock, J. S., Strigari, L. E., & Willman, B. 2008, *ApJ*, 688, 277, 0806.4381
 van den Bergh, S. 1972, *ApJ*, 171, L31+
 van der Marel, R. P., & Guhathakurta, P. 2008, *ApJ*, 678, 187, 0709.3747

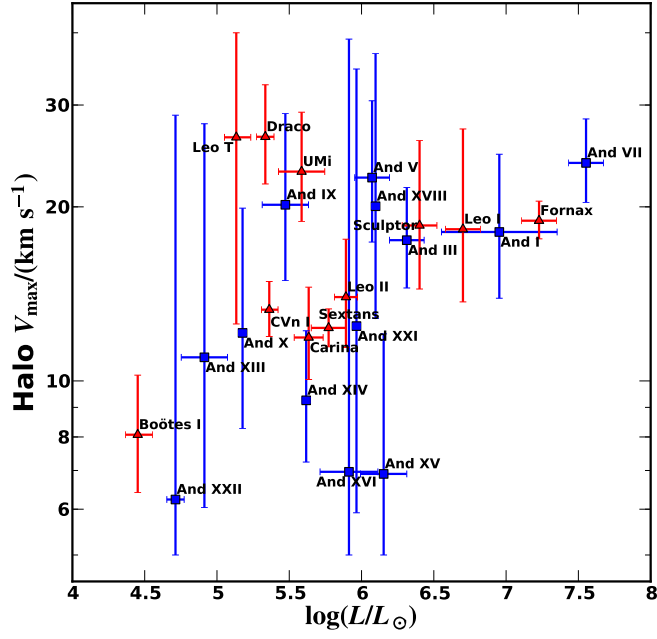


FIG. 25.— Maximum circular velocity of an NFW halo inferred from dSph scalings as a function of luminosity. The V_{max} values are computed based on the satellite's location in the R - M plane as described in the text. Points (blue) are M31 dSphs, while triangles (red) are MW dSph satellites.

- Walker, M. G., Mateo, M., Olszewski, E. W., Gnedin, O. Y., Wang, X., Sen, B., & Woodroffe, M. 2007, *ApJ*, 667, L53, 0708.0010
- Walker, M. G., Mateo, M., Olszewski, E. W., Peñarrubia, J., Wyn Evans, N., & Gilmore, G. 2009, *ApJ*, 704, 1274, 0906.0341
- Watkins, L. L., Evans, N. W., & An, J. H. 2010, *MNRAS*, 406, 264, 1002.4565
- Wolf, J., Martinez, G. D., Bullock, J. S., Kaplinghat, M., Geha, M., Muñoz, R. R., Simon, J. D., & Avedo, F. F. 2010, *MNRAS*, 406, 1220, 0908.2995
- Zucker, D. B. et al. 2004, *ApJ*, 612, L121, arXiv:astro-ph/0404268
- . 2007, *ApJ*, 659, L21, arXiv:astro-ph/0601599